LA-9247-MS

Los Alamos National Laboratory is operated by the University of California for the United States Department of Energy under contract W-7405-ENG-36.

Antares Phase Two

October 1980

Los Alamos Los Alamos National Laboratory
Los Alamos, New Mexico 87545

DISCLAIMER

This work was supported by the US Department of Energy, Office of Laser Fusion.

Edited by Betty Leffler
Photocomposition by Samia L. Davis
Assisted by Jo Ann Painter

LA-9247-MS

UC-21
Issued: May 1982

LA--9247-MS

DE82 016241

Antares Phase Two

October 1980

W. T. Leland
M. Kircher
E. Sklar
E. Yavornik
V. Zeigner

Los Alamos National Laboratory
Los Alamos, New Mexico 87545

CONTENTS

ANTARES PHASE TWO
October 1980

by

W. T. Leland, M. Kircher, E. Sklar, E. Yavornik, and V. Zeigner

ABSTRACT

Definition of a large CO_2 laser system that would fit into the Antares facility was undertaken. Described here are the five amplifier cross sections that were studied, seven target systems, focusability and optic quality, and the crosstalk that occurs in muliplexed amplifiers. Eight amplifier system options are described: three are 400 kJ, five are 200 kJ, and one of each of these is multiplexed. A cost analysis is presented as an aid in comparing the options, and the current Antares design and a design-modification are reviewed.

Two novel features have led to 400-kJ options that fit into the Antares facility. The first is the concept of a saturated-two-pass amplifier wherein substantial energy is picked up on the first pass and full benefit of fast gain recovery is utilized on the second pass. This feature leads to a smaller, more efficient amplifier. The second feature, the extensive use of solid dielectric insulation in the discharge chamber, also leads to size reduction and cost saving.

I. INTRODUCTION

The objective of the Antares Phase Two (APT) task group is the definition of a viable large CO_2 laser system that could be implemented in the Antares facility. To accomplish this objective we have divided the work into two tasks. The first task was to define the limitations imposed by the existing physical plant, the state-of-the-art technology, and the target design criteria and to develop in general terms a slate of option candidates from which to choose the finalist(s) for further study. The second task would provide a proposal for Antares upgrade.

The study reported here also includes a review of the current Antares design. Two amplifiers are under construction, and completion of the full six-amplifier complex is an option that can be considered.

The official task group consists of Jack C. Comly, Jr, (X-1), Mary Kircher (L-10), Charles Knapp (L-10), Wallace Leland (L-10), Edward Sklar (L-10), Edward Yavornik (L-10), and Vernon Zeigner (L-10).*

Almost all effort was devoted to studies of the target system, the power amplifier system, and the associated large optics. Apart from very cursory examination and some crude cost estimates based on Antares experience, no considerations have been given to the energy storage, controls, integrated optics, or front-end systems.

The usual problems of parasitics and retropulse were not considered in detail. The design gain-length products are at levels believed viable for amplifiers not requiring saturable absorbers for stability and except for the study

*L-10 designates a group existing before Los Alamos National Laboratory reorganization in 1981.

of Antares, no saturable absorbers are included in the designs.

Several design criteria have evolved in connection with the limitations mentioned above.

- No "major" revisions to the target building should be considered.
- Modifications to other buildings are not ruled out. Additional buildings may be considered.
- "New" designs should exceed 180 kJ.
- Efficiency is not a prime consideration.
- Six to eight clusters of beams are permitted. Less than 50 μJ prepulse energy per cluster is required.
- Pulse length is up to 2 ns.
- There should be 200 shots between major retrofits.
- Target spot size requires 80% energy in 400-μm diameter.
- Salt loading may be up to 2.5 $\sqrt{t}$ J/cm^2 with t in nanoseconds.
- Mirror loading may be 5 $\sqrt{t}$ j/cm^2.
- Salt diameter may be 18 in. maximum.
- Low-powered salt may be used.
- For diamond-turned mirrors, swing radii on the order of 100 in. are permitted.

Five amplifier cross sections were studied and are described in Sec. II. Seven target systems designs are described in Sec. III. Considerable attention was given to crosstalk, which is a serious concern in multiplexed systems. Section IV covers this subject, as well as the usual focusability and optic quality determinations. Eight system options (three 400 kJ and five 200 kJ) are described in Sec. V. The cost analysis for the conceptual system designs given in Sec. VI is based largely on Antares experience and is intended as an aid in comparing the options. All major identified components are costed accurately. Unspecified parts and labor costs based on Antares experience also are included.

Two novel features have led to 400-kJ options that fit into the Antares facility and at the same time reduce the estimated cost per joule substantially. One is the concept of a "saturated-two-pass amplifier" wherein substantial energy is picked up on the first pass and full benefit of fast gain recovery is utilized on the second pass. This feature leads to a smaller, more efficient amplifier. Likewise, the extensive use of solid dielectric insulation in the discharge chamber as opposed to the usual gas dielectric material has allowed substantial size reduction and cost saving.

II. POWER AMPLIFIER

A. Amplifier Cross-Section Area

To discuss the amplifier size it is convenient to introduce the term "beamlet." From the target system point of view, each beamlet represents a beam of coherent phase and total energy E_B. Each beamlet requires a separate final focusing optic and follows a separate path throughout the target system. The total energy E_T and the number of required beamlets N are related to E_B by

$$E_T = NE_B \ .$$

To attain the desired spot size, the solid angle subtended by each beamlet at this final focusing optic must exceed some minimum value ($d\Omega_{min}$). This sets an upper limit to the number of beamlets that can be used.

$$N_{max} = \frac{\alpha 4\pi}{d\Omega_{min}} \ ,$$

where α is the fraction of solid angle available to the final focusing optic.

For a 400-μm spot size the final optic corresponds to f/15.5 for diffraction-limited beamlet quality. Choosing f/10 as appropriate for Antares-like beam quality and taking α equal to 0.1 gives N_{max} of roughly 160. Using the maximum number of beamlets corresponds to smallest permissible amplifier output E_A. It follows that

$$E_A\,(\text{min}) = \frac{E_T}{N_{max}} \ ,$$

where it has been assumed that the output of more than one amplifier cannot reasonably combine to give a coherent beamlet. In the range $200 \leq E_T \leq 400$ kJ, E_A(min) varies from 1.25 to 2.5 kJ. There is, of course, no restriction on using fewer but larger beamlets. The limitation on using larger beamlets comes from practical considerations in making the "largest" amplifier.

The number of amplifiers required can be fewer than the number of beamlets if multiplexing is used, but the target system still must supply one beam path per beamlet.

The cross-sectional area of each beamlet is constrained to be large enough to avoid damage (2.5 J/cm^2 at salt windows and 5 J/cm^2 at copper mirrors)* and to subtend $d\Omega_{min}$ at the final focus element.

At the amplifier, the cross-sectional area is restricted by the 2.5 J/cm^2 salt window limitation unless optical magnification is used between the amplifier and salt window. The latter alternative has not been considered because, apart from the added complication of more powered optics, it entails additional dead-gas space and higher gain length (gL) product to obtain the output energy density. The largest amplifier cross section considered is 46 by 46 cm, the size needed to fill an 18 in.-diam salt window (16.5-in. clear aperture). Uniform loading at 2.5 J/cm^2 gives an output of 3.45 kJ.

With the above considerations, the range of amplifier cross sections is relatively limited, as shown in Table I. Amplifier No. 1 uses an 18-in. salt (16.5-in. clear aperture) and produces a circular beam completely filling the aperture. Amplifier No. 2 also produces a circular beam and is the smallest unit giving 400 kJ under the limitation of no more than 160 beamlets. Amplifier No. 3 minimizes the discharge size by producing a square beam. The circle size to circumscribe the square beam becomes quite large, 17.6 in., which would require more than an 18-in. salt. For 200 kJ even smaller amplifiers will suffice as indicated by entries 4 and 5 in the table. Entries 1, 2, and 3 are attractive in that the choice of 200 or 400 kJ is reflected only in the number of amplifiers required.

B. Beam Uniformity

Nonuniform ionization by primary electrons and magnetic field effects make uniform beams impossible in large amplifiers. Magnetic problems can be alleviated by using low discharge currents and compensating the sacrifice in g by making the amplifier longer. Using a Helios-like "B_z" configuration for current return is generally better than using the Antares "B_θ" arrangement. All designs considered use the B_z configuration. Amplifiers in the range shown in Table I were analyzed for discharge power deposition, and the ratio of average to peak is noted as a figure of merit. Using only values in the beam extraction area improved the expected performance somewhat in the case of circular beams because the corners tend to be poor. Shaping the anode improved uniformity in many cases. Results of these calculations are given in Tables II, III, and IV. In Tables III and IV, curvature refers to the decrease (in cm) of anode-to-cathode spacing at the outer edge of the discharge.

The question, "What is the maximum nonuniformity that can be allowed?" is not readily answered. Ultimately, the concentration of electric field will lead to breakdown, but a more important consideration, in most cases, will be the effect on the window damage-system performance tradeoff. The 2.5 J/cm^2 specification at 1 ns presumably should scale to $\sqrt{2} \times 2.5$ for a 2-ns pulse. This represents a 40% contingency for the nominal 2.5 J/cm^2 designs considered and, in principle, a uniformity figure of merit as low as 0.6 could be tolerated. Tables III and IV show that, with curved anodes and current densities of 10, figure of merit values ~0.8 can be expected.

C. Amplifier Efficiency: Saturated-Two-Pass and Multiplex Considerations

The gain recovery predicted by kinetics now used (but not verified by direct experiments) indicates that significant recovery will occur in 10-20 ns for amplifier conditions of interest. This fast recovery can be utilized to enhance the performance significantly if a saturated-two-pass system is used. Sizable amounts of energy must be extracted on the first saturated pass to benefit from this scheme. The major problem is getting good volume utilization on the first pass, which also must be an expanding pass. A study was performed on an 1800-torr 1:4 (N_2:CO_2) amplifier 200 cm long with a 31.6- by 31.6-cm area. The expanding pass had a radius of 7.62 cm at the entrance to the gain medium and 14 cm at the exit. The final output beam had a radius of 15.8 cm and occurred with 15-ns delay. The results of the study are shown in Table V. The study suggests that a design with g = 3.5%/cm and a two-pass energy gain of 37 would give the nominal 2.5 J/cm^2 output. The total drive for a 400-kJ system thus would be 10.8 kJ. If a third pass were used, an additional power gain on the order of 400 would be realized and the total drive would be reduced to ~27 J.

*In accordance with the given criteria, these numbers could be increased by 41% for a 2-ns pulse. This increase was considered as a reasonable design margin to accommodate nonuniformities.

TABLE I. Amplifier Options

Amplifier No.	Usable Discharge (cm)	Circular Window Clear Aperture (in.)	Configuration[a]	No. Required 200 kJ	No. Required 400 kJ
1	41.9 by 41.9	16.5		58	116
2	35.7 by 35.7	14.0		80	160
3	31.6 by 31.6	17.6		80	160
4	25.2 by 25.2	9.9		160	---
5	22.4 by 22.4	12.45		160	---

[a]The circle denotes optical window size and the square the discharge size. When the discharge "square" is encircled by the window, the output beam would not be circular.

TABLE II. Uniformity Figure of Merit $\bar{P}/P_{max}$ Versus j and Amplifier Size

	Amplifier Size (cm)	Beam Shape	j = 0	j = 3	j = 6	j = 10	j = 15
1800 torr 1:4 (N_2:CO_2)	46 by 46	circle	0.90	0.86	0.80	0.72	0.60
	37 by 37	circle	0.90	0.88	0.82	0.78	0.72
	25 by 25	circle	---	0.91	0.88	0.85	---
	25 by 25	square	---	0.89	0.85	0.81	---
2400 torr 1:4 (N_2:CO_2)	46 by 46	circle	---	0.84	0.75	0.66	0.60
	37 by 37	circle	---	0.86	0.81	0.76	0.71
	25 by 25	circle	---	0.91	0.87	0.85	0.82
	25 by 25	square	---	0.88	0.83	0.81	0.77

To obtain an output of 2.5 J/cm^2 in single-pass operation, a gL of 9.14 would be required. The efficiency gain is ~9.14/7 = 1.31.

Driven by an energy supply with similar time history of current and voltage to that used in Antares, the required stored energy for a 400-kJ system is ~1.72 × 10^7 J.

Multiplexed amplifiers offer another approach to improve efficiency. A major problem confronting this design is crosstalk arising from diffraction or scattering. The problem is addressed in Sec. IV.

It is not possible to guarantee a contrast ratio of 10^9 or more without using unrealistically large angles between beams. With large angles between beams, the wasted amplifier volume becomes large, and without larger windows, adequate-size beams are difficult to arrange. A design study was performed with 2° between beams and four beamlets created by each amplifier. Additional isolation between beams could be obtained with saturable absorbers in each output beamlet path, but would reduce the efficiency and add to the complexity. The choice of four beamlets per amplifier is arbitrary. A smaller multiplicity improves amplifier efficiency only minimally, while greater multiplicity forces amplifier size to exceed sizes that are feasible with presently available salt windows.

The kinetics of a "four-plexed" amplifier has been examined. Three helium-free mixtures were considered:

TABLE III. Effect of Anode Curvature on Figure of Merit $\bar{P}/P_{max}$: 1800 torr 1:4 (N_2:CO_2)

Amplifier Size (cm)	j	Curvature 0	2	4	6	8
46 by 46	0	0.90	0.89	0.87	---	---
	3	0.86	0.89	0.91	0.91	0.91
	6	0.80	0.82	0.84	0.86	0.87
	10	0.72	0.74	0.75	0.77	0.78
	15	0.60	0.62	0.64	0.66	0.67
37 by 37	0	0.90	0.94	0.92	0.89	---
	3	0.88	0.93	0.94	0.93	---
	6	0.82	0.86	0.90	0.92	---
	10	0.78	0.82	0.85	0.87	---
	15	0.72	0.75	0.78	0.80	---
25 by 25						
circle	3	0.91	0.94	0.91	---	---
square	3	0.89	0.92	0.91	---	---
circle	6	0.88	0.93	0.90	---	---
square	6	0.85	0.91	0.90	---	---
circle	10	0.85	0.91	0.92	---	---
square	10	0.81	0.87	0.90	---	---

TABLE IV. Effect of Anode Curvature on Figure of Merit $\bar{P}/P_{max}$ 2400 torr 1:4 (N_2:CO_2)

Amplifier Size (cm)	j	Curvature 0	2	4	6	8
46 by 46	3	0.84	0.86	0.87	0.87	0.88
	6	0.75	0.77	0.79	0.81	0.84
	10	0.66	0.68	0.70	0.71	0.73
	15	0.60	0.62	0.64	0.65	0.66
37 by 37	3	0.86	0.90	0.92	0.92	---
	6	0.81	0.85	0.87	0.88	---
	10	0.76	0.79	0.82	0.85	---
	15	0.71	0.74	0.76	0.79	---
25 by 25						
circle	3	0.91	0.91	0.90	---	---
square	3	0.88	0.89	0.90	---	---
circle	6	0.87	0.93	0.93	---	---
square	6	0.83	0.91	0.92	---	---
circle	10	0.85	0.90	0.93	---	---
square	10	0.81	0.86	0.91	---	---
circle	15	0.82	0.87	0.90	---	---
square	15	0.77	0.83	0.87	---	---

TABLE V. Saturated Two-Pass Amplifier Performance

E_{in} (J)	E_{out} (J/cm^2)/Power Gain g = 3%/cm	g = 3.5%/cm	g = 4%/cm
26.3	2.10/61.4	2.42/72.2	2.79/83.2
52.5	2.13/31.8	2.49/37.1	2.84/42.3
78.8	2.17/21.6	2.53/25.2	2.89/28.8

1:1, 1:2, and 1:4 (N_2:CO_2). Mixtures containing helium undoubtedly would be satisfactory, but the need to keep magnetic fields low definitely favors mixtures that operate at higher E/N and lower j. Typical results are shown in Figs. 1-4. These results were among the best produced in the study, which included variations both of extraction time for the first pulse and of the interval between pulses. The discharge was an amplitude-scaled version of a calculated Antares case. In each case shown, the pressure is 1800 torr. Because the discharge is long compared to relaxation times, substantial gain recovery is obtained from the continued pumping, but to utilize this feature, the delays between pulses must be lengthened. Further equalization of gain for each pulse could be achieved by varying the time interval between pulses or by varying the input for each pulse. Of the three mixtures considered, the 1:2 performed best. The overall amplifier length must be increased to compensate for the lower gain. Assuming a 3-m amplifier of 46- by 46-cm cross section and Antares-like discharges, we estimate the necessary stored energy to be 1.2×10^7 for a 400-kJ system.

Drive considerations are similar to the saturated two pass, except for the added complexity of introducing delays between the pulses.

D. Discharge Chamber Design

The overall cross-sectional area of the amplifiers used in Antares and Helios is quite large. Their cross sections are two to three times the anode-to-cathode spacing. This large size is required because laser gas is used for electrical insulation in regions of low ionization. For a 400-kJ design, the volume of the present Laser Hall could not accommodate such large units.

A proposed, more compact design uses plastic instead of laser gas for insulation. The usual problem of voids

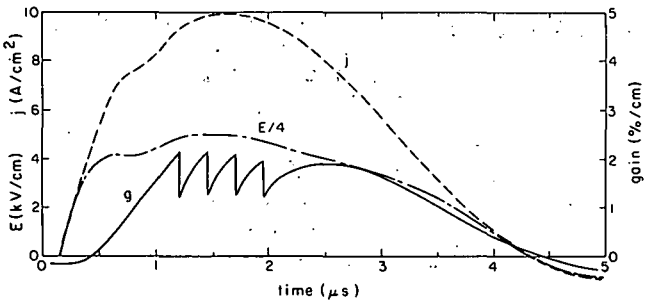

Fig. 1. Electric field, current density, and small signal gain for a 1:4 (N_2:CO_2) mix at 1800 torr. The inversion was removed completely four times, at 1.2, 1.45, 1.7, and 1.95 μs.

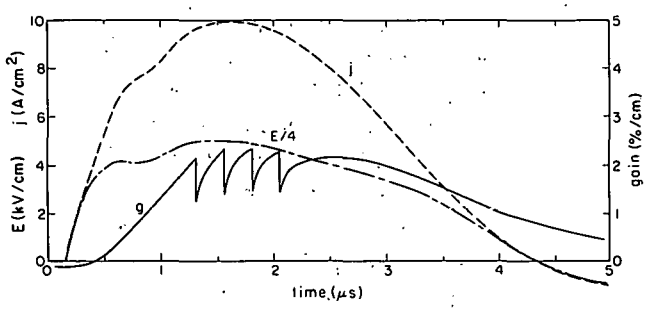

Fig. 2. Electric field, current density, and small signal gain for a 1:1 (N_2:CO_2) mix at 1800 torr. The inversion was removed completely four times, at 1.3, 1.55, 1.8, and 2.05 μs.

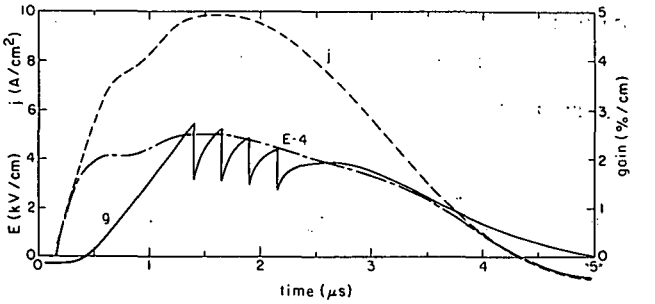

Fig. 3. Electric field, current density, and small signal gain for a 1:2 (N_2:CO_2) mix at 1800 torr. The inversion was removed completely four times, at 1.4, 1.65, 1.9, and 2.15 μs.

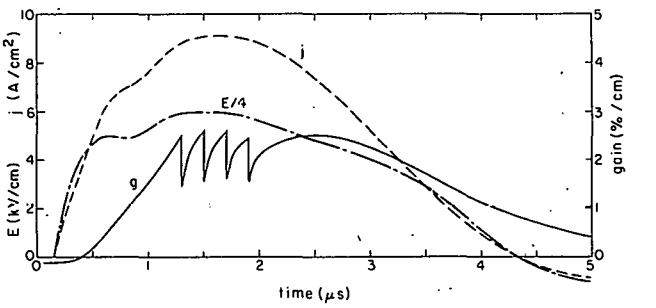

Fig. 4. Electric field, current density, and small signal gain for a 1:1 (N_2:CO_2) mix at 1800 torr. The inversion was removed completely four times, at 1.3, 1.5, 1.7, and 1.9 μs.

inadvertently occurring in the plastic-to-wall or plastic-to-electrode interfaces is eliminated by spraying a metal coating onto the plastic where it must meet metal. It is possible to produce the necessary plastic castings and apply the conducting coatings using capabilities available at Los Alamos.

E. Amplifier Packaging

The proposed discharge chamber design is shown in Fig. 5. The amplifier is much smaller overall and allows accommodation of a 400-kJ system in the present Laser Hall. The size reduction also results in a substantial cost reduction.

Rectangular and cylindrical packaging schemes were considered. They are illustrated in Figs. 6 and 7. With the heights of packages limited by the crane hook height, the rectangular arrangement proved more amenable to fitting packages into the existing building. Figures 6 and 7 each show eight amplifiers assembled in one package. This is the maximum nunber reasonable in a cylindrical configuration. With the rectangular arrangement, the number of amplifiers per package can be 14 or more.

III. TARGET SYSTEM ARRANGEMENTS FOR APT

Seven arrangements of target focus systems have been examined. They fall into three groups differentiated by the geometries of mirror placement. The following assumptions were made in all seven cases.

- All individual beams are circular.
- All beam arrays, regardless of beam size or number, are made as nearly circular as possible.
- The present target chamber can be replaced, but the existing bridge crane and hook height must be respected.
- Target building walls cannot be moved.
- Beam tube holes in the target building wall may be enlarged.

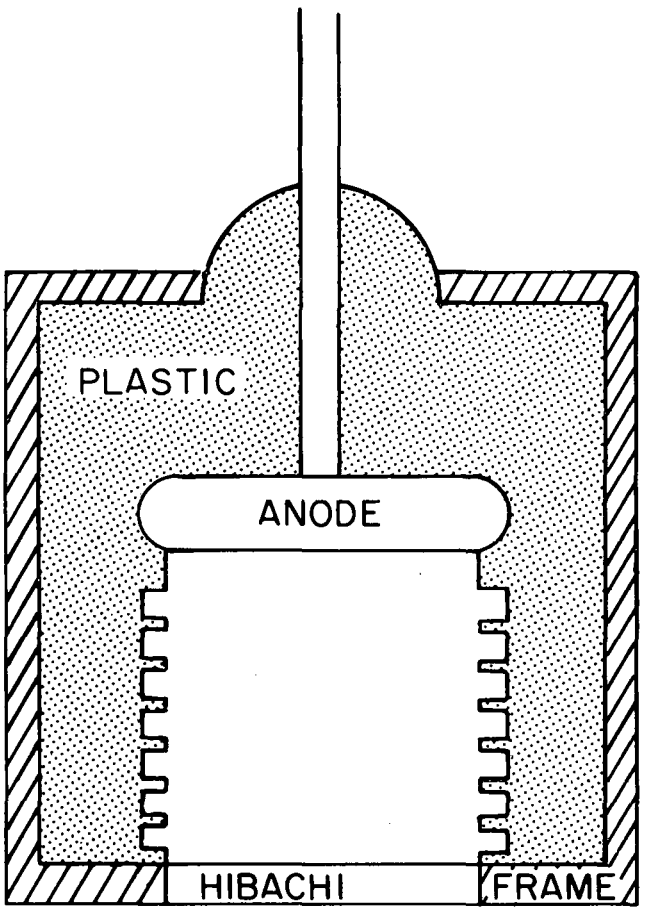

Fig. 5. Cross section of the compact discharge chamber design proposed for APT.

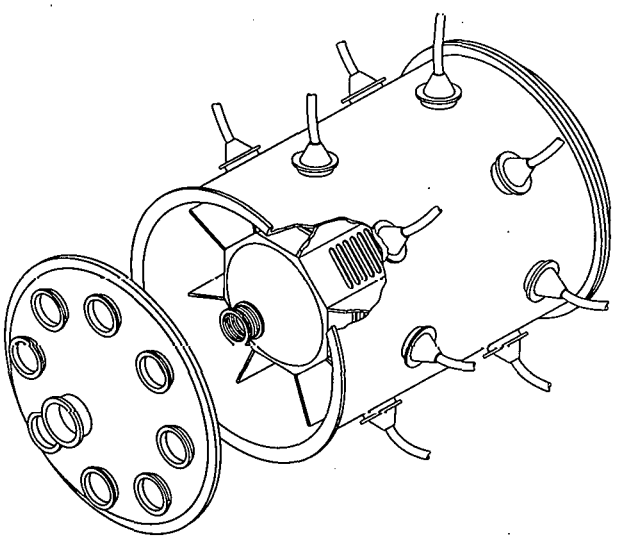

Fig. 6. Cylindrical packaging of eight amplifiers with current returns between segments.

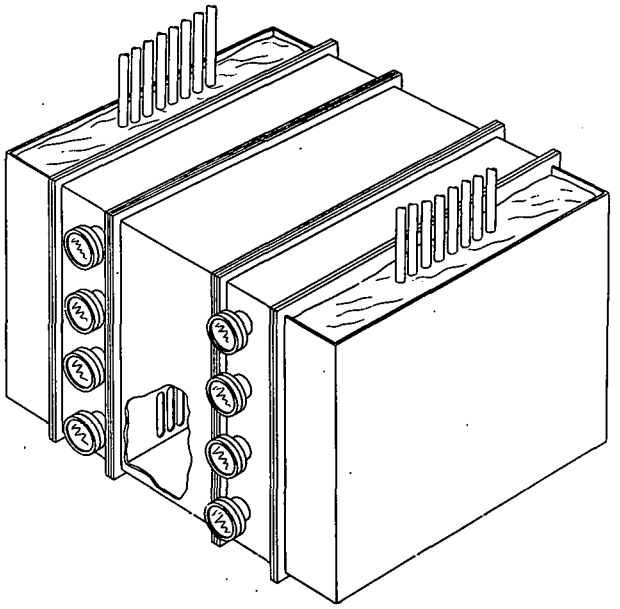

Fig. 7. Rectangular packaging of eight amplifiers. A common two-sided E-gun is located between the two discharge chamber arrays. An outer oil-filled tank houses the cable terminations.

- Turn-mirror locations can be varied, but caution must be used.
- Focus arrangements ignore convergence of individual beams or beam arrays. These convergences have a secondary effect on target chamber size.
- All focus mirrors are sized to have fluence of 5 J/cm^2.
- Swing radii for diamond-turned mirrors of ~100 in. are permitted.

Six bundles of beamlets are used in the full Antares design. Three bundles approach the target from three turning mirror arrays grouped at the east end of the target building and three bundles approach from three turning mirror arrays at the west end of the building. For descriptive purposes, a horizontal east-west line through the target is designated as the X-axis. The target is placed at the coordinate system origin, and the Y-Z plane is placed at a vertical north-south orientation.

The basic optics layout for a Group I system is shown in Fig. 8. An artist's sketch, which uses this arrangement, is shown in Fig. 9. The distinguishing features of this group are

- turn mirrors at present location,
- no fold mirrors,
- passage of beams through the Y-Z plane on way to focus mirrors, and
- a purely cubic focus arrangement so that pairs of focused arrays "see" each other.

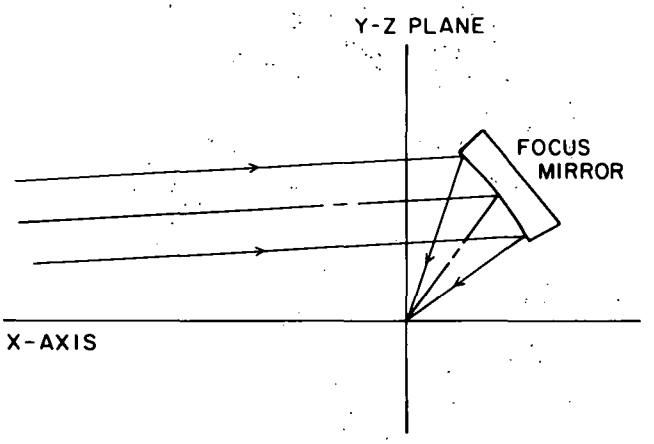

Fig. 8. Location of focus mirror and target for a Group I target system.

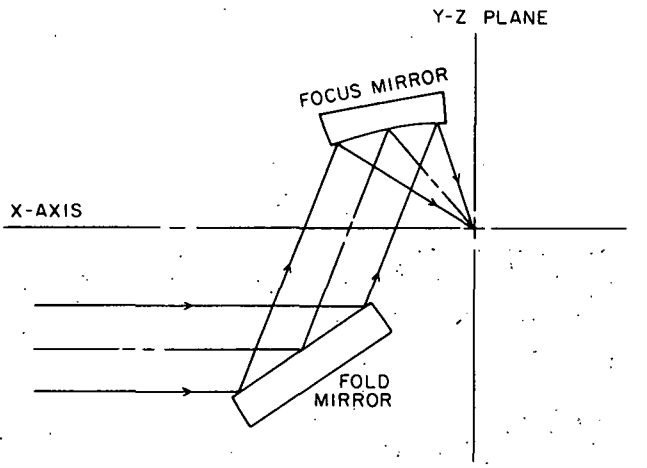

Fig. 10. Location of focus mirror, turn mirror, and target for a Group II target system.

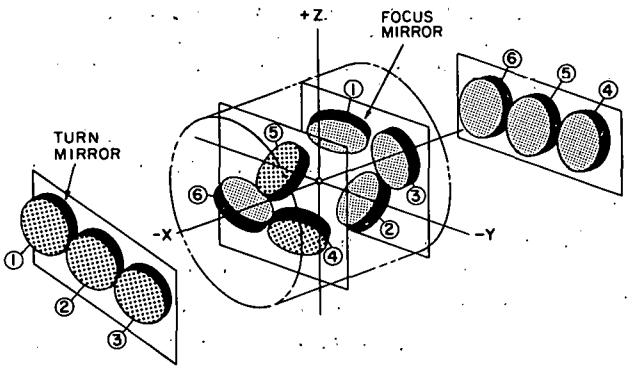

Fig. 9. Artist's sketch of turn and focus mirror locations for a Group I target system.

The basic optics layout for a Group II system is shown in Fig. 10. Artist's sketches for design No. 4, which uses this arrangement, are shown in Figs. 11a-c. The distinguishing features of this group are

- turn mirrors at present locations,
- fold and focus mirrors on same side of the Y-Z plane as their respective turn mirrors, and
- a modified cubic focus arrangement as in Antares I, so that pairs of focused arrays do not see each other.

The basic optics layout for a Group III system is shown in Fig. 12. An artist's sketch for design No. 7, which uses this arrangement, is shown in Fig. 13. The distinguishing features of this group are

- No. 2 and No. 5 turn mirrors are lifted ~120 in.,
- no fold mirrors,
- focus mirrors on same side of the Y-Z plane as their respective turn mirrors, and
- a modified cubic focus arrangement as in Antares I.

In all three groups, the surfaces of focus mirrors in each array lie on a parabolic surface. Each group differs in the relative part of the parabolic surface utilized.

The three groups of arrangements were examined in some detail for one to three designs. The designs differed in the number and size of individual beam used and, therefore, in the total system energy. Information on the number of beamlets, size, and group for each design is given in Table VI. The intent of the examination was to determine the magnitude of various parameters, such as

- array diameter.
- array cone angle.
- target approach angle (angle median x-ray of bundle makes with X-axis).
- swing radius for machining focus parabolas.
- target chamber diameter.
- target chamber length.
- range of f-numbers for the various focus mirrors.

In all cases, a reasonable effort was made to lay out geometries that provided some consistency in considerations, such as

- clearance between mirrors and Y-Z plane.
- clearance between mirror arrays and passing beams.
- clearance between beams approaching the target chamber from the turn mirrors. (*Note:* This was *not* achieved in Design No. 7.)

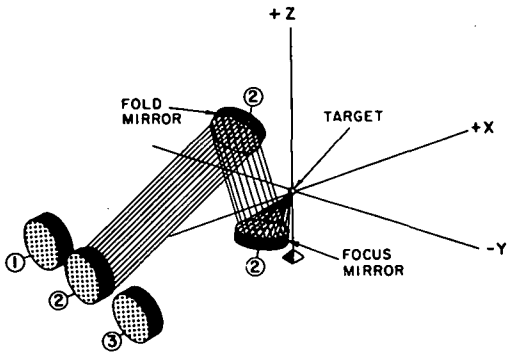

Fig. 11a. Artist's sketch of turn, fold, and focus mirror locations for beam 2 for a Group II target system.

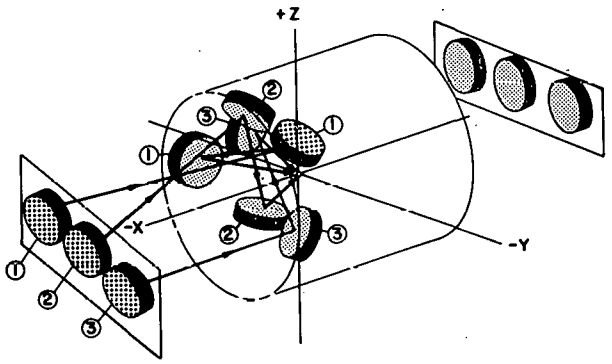

Fig. 11b. Artist's sketch of the turn, fold, and focus mirrors for beams 1, 2, and 3 for a Group II target system.

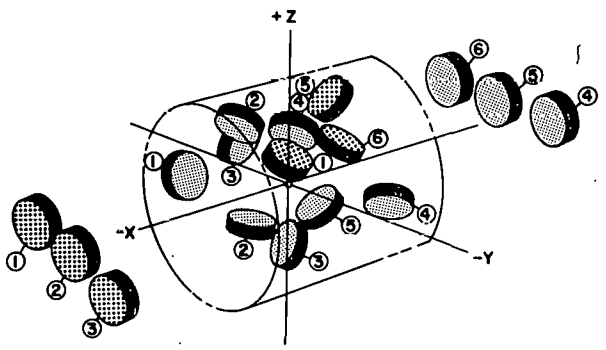

Fig. 11c. Artist's sketch of the turn, fold, and focus mirrors for all six beams for a Group II target system.

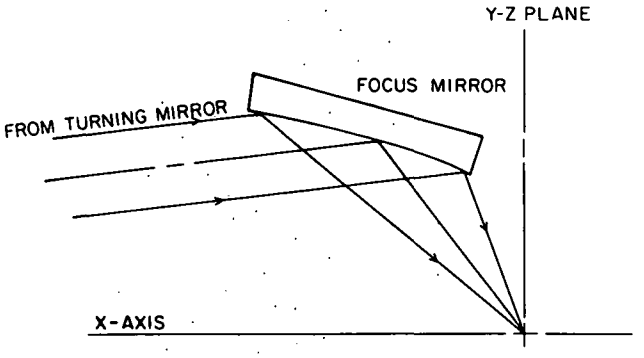

Fig. 12. Location of focus mirror and target for a Group III target system.

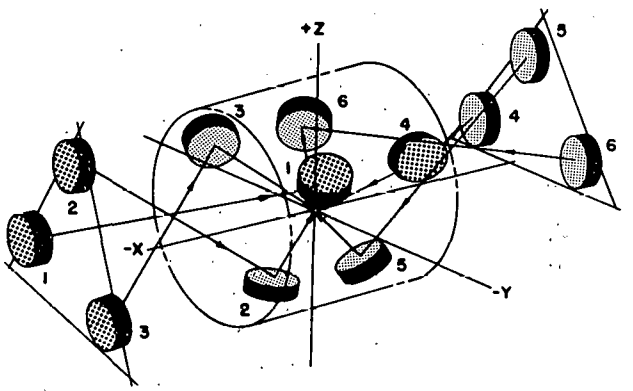

Fig. 13. Artist's sketch of the turn and focus mirrors for a Group III target system.

TABLE VI. Target Focus Systems

Group	Design No.	Beam Diam at Focus Mirror (in.)	Total No. of Beams
I	1	10	168
	2	12	72
	3	12	114
II	4	10	168
	5	12	72
	6	12	114
III	7	10	168

- target approach angle being kept within 5° of the Antares six-beam system's value of 54.7°.
- clearance between individual beams within an array.

Beam array diameters were selected for the numbers of beams used in each array according to the following rules.

- Center-to-center spacing of beams within an array is 1.5 in. greater than the beam diameter.
- Beams are arranged in arcs having a common center approximately where the machining axis for a focus parabola would be. This minimizes the number of different mirrors to be stocked.

This procedure provided beam arrays as shown in Figs. 14-16. The results of this study are presented in Tables VII and VIII. The tables provide input data and the following parameters.

- Range of f-number.
- Target approach angle.
- Array cone angle.
- Target chamber diameter.
- Target chamber length.
- Swing radius.

Table VIII also shows a summary of other factors that may be helpful in comparing the different designs.

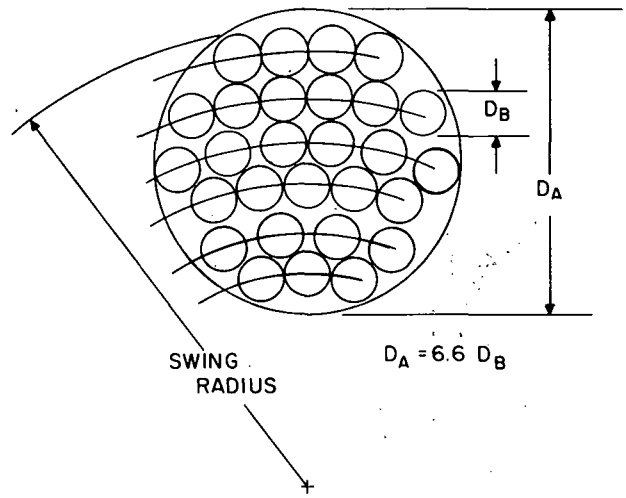

Fig. 14. Mirror array for 28 beams.

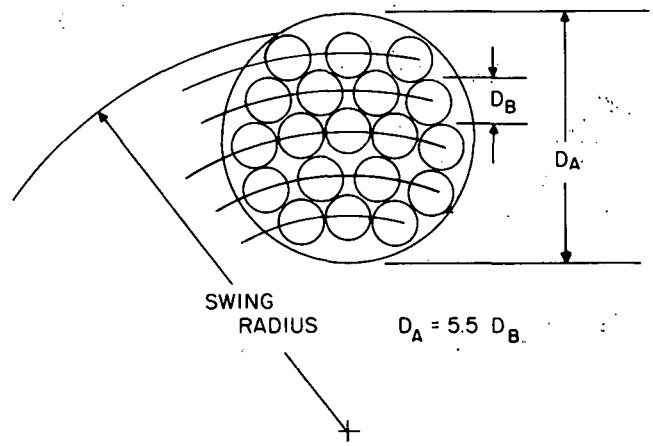

Fig. 15. Mirror array for 19 beams.

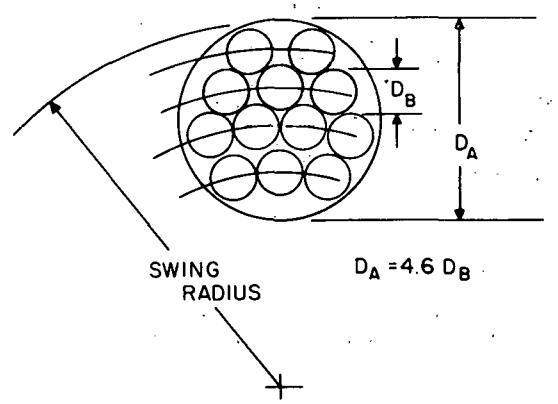

Fig. 16. Mirror array for 12 beams.

IV. OPTICS

A. Crosstalk

Multiplexing a CO_2 laser system is an attempt to increase overall system efficiency by passing several beams through the same gain medium. The beams are spread in time by an amount required to extract significantly more total energy from the gas than can be extracted by one pass. Difficulty arises from a severe limitation on energy arriving on target before the main pulse arrives. Crosstalk, in the form of diffraction from a finite aperture (common to several beams) or scatter from a window or mirror, can cause energy to arrive on target by a shorter path than that of the main pulse. Several methods were used to estimate the magnitude of crosstalk from diffraction and scattering.

1. Diffraction

a. Perfect Wave Front Through a Round Aperture. The crosstalk between two perfect beams passing through the same circular aperture is estimated by

TABLE VII. Details of Target Focus Systems

	Design No.						
	1	2	3	4	5	6	7
System energy (kJ)	400	260	400	400	260	400	400
No. of beams	168	72	114	168	72	114	168
Beam diam (in.)	10	12	12	10	12	12	10
Beam array diam (in.)	75	56	66	75	56	66	75
f/number	7-12	6-9	7-9	8-12	6-8	6-9	5-16
Target approach angle (°)	55	55	55	51	51	51	55
Array cone angle (°)	40	33	38	42	42	42	44
Target chamber diam (ft)	22-24	20	22	28-30	22	24-25	20
Target chamber length (ft)	16	16	16	25	25	25	22-24
Swing radius (in.)	110	94	104	107	98	105	127

TABLE VIII. Features of Target Focus Systems

	Design No.						
	1	2	3	4	5	6	7
Focused arrays see each other	yes	yes	yes	no	no	no	no
Beams compressed after salt	yes	yes	yes	yes	yes	yes	yes
Target chamber changes							
diam	no	no	no	yes	no	yes	no
length	yes[a]	yes[a]	yes[a]	yes	yes	yes	yes[b]
Turn-chamber changes	yes	prob.	prob.	yes	prob.	prob.	yes[b]
Larger beam tubes at							
south wall of target bldg.	yes	maybe[c]	maybe[c]	yes	maybe[c]	maybe[c]	maybe[c,d]

[a]On the present east end of the chamber, which is 26 in. shorter than the west end.

[b]Complications result in target chamber, turn chamber, and beam tube interfaces because beams cross the X-Y plane between the turn and focus mirrors.

[c]Depends upon where the beam and array diameters are reduced.

[d]Holes No. 2 and 5 would have to be moved upward.

calculating the far-field diffraction pattern for large angles of observation. The far-field pattern is an analytic solution to the scalar wave equation under far-field conditions. It is appropriate because the angles are relatively small (6° at most) and the aperture is several thousand wavelengths in size.

The geometry is shown in Fig. 17. Two beams pass through a common aperture or optic of diameter d, and a fraction $I(\theta)$ of the energy in beam 1 appears in beam 2. We have[1]

$$I(\theta) = \left[\frac{2\,J_1(X)}{X}\right]^2, \qquad (1)$$

where $X = \pi \sin\theta\, d/\lambda$ and d is the diameter.

When X is large, $J_1(X) = F_1 \cos\theta/X^{0.5}$, where F_1, the original f-number, is

$$F_1 = 0.797\,884\,56 + 0.000\,001\,56\left(\frac{3}{X}\right) + \ldots .$$

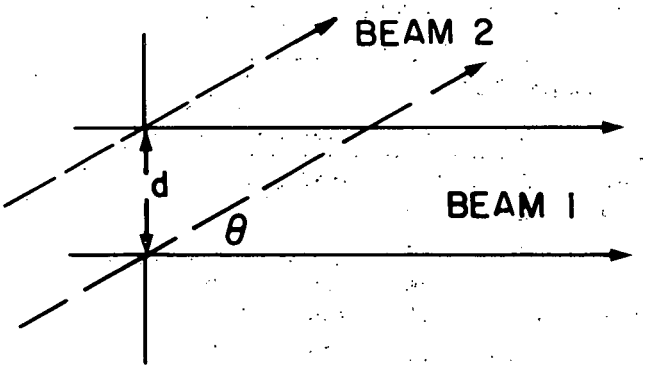

Fig. 17. Geometry for crosstalk considerations.

For large X and because $\cos^2\theta$ is ≤ 1,

$$I(\theta) \leq \frac{2.546\,479\,08}{X^3} . \qquad (2)$$

When $\lambda = 0.010$ mm and $d = 400$ mm (16 in.), then $X = 1.256\,64 \times 10^5 \sin\theta$. For $I(\theta) = 10^{-12}$, $\theta \simeq 110$ mrad (6.2°). Similarly, $\theta \simeq 11$ mrad (0.62°) for $I(\theta) = 10^{-9}$.

b. Small Phase Errors Over a Round Aperture. The far-field pattern approach was extended to wave fronts with small, rotationally symmetric phase errors. The result is approximated for large angles with the rather weak conditions that the phase error vary slowly and that the higher derivatives of the phase error be reasonable. The significant conclusion is that for large angles and small phase errors of low spatial frequency, the crosstalk does not differ significantly from that of a perfect wave front. A physical interpretation of this phenomenon is that while low-frequency phase errors remove energy from the core of the pattern, most of this energy is redistributed into the first few rings and is not sent in the direction of the thousandth ring (large angle).

For a circular wave front characterized by a phase function $W(y)/\lambda$ with $0 \leq y \leq 1$,

$$I(\theta) = \left[2 \int_0^1 \exp\left[2\pi i W(y)/\lambda\right] J_0(Xy) y\,dy \right]^2 . \qquad (3)$$

An asymptotic expansion of this integral is given in the appendix. Using Eq (A-10) from there we have

$$I(\theta) \cong 4 \left\{ \exp\left[2\pi i W(1)/\lambda\right] \times \left[\frac{J_1(X)}{X} + \frac{2\pi i}{\lambda} \frac{J_0(X)}{X^3} \frac{dW}{dy}\bigg|_{y=1} \right] \right\}^2$$

$$= 4 \left\{ \left[\frac{J_1(X)}{X} \right]^2 + \left[\frac{2\pi}{\lambda} \frac{J_0(X)}{X^3} \frac{dW}{dy} \right] \right\}^2 . \qquad (4)$$

When $\sin\theta = 0.1$, $d = 400$ mm, and $\lambda = 0.01$ mm, then X is 1.26×10^4 and

$$I(5.7°) \cong 2.53 \times 10^{-8} J_1^2(1.26 \times 10^4) + 4.01 \times 10^{-19} \left(\frac{dW}{dy} \right)_{y=1}^2 J_0^2(1.26 \times 10^4) . \qquad (5)$$

For large arguments (p. 370)

$$J_0^2(Z) = \frac{2}{\pi Z} \cos^2(Z - \pi/4) , \qquad (6)$$

$$J_1^2(Z) = \frac{2}{\pi Z} \cos^2(Z - 3\pi/4) , \qquad (7)$$

and Eq (5) becomes

$$I(5.7°) \cong 1.3 \times 10^{-12} \cos^2(X - 3\pi/4) + 2 \times 10^{-23} \left(\frac{dW}{dy} \right)_{y=1}^2 \cos^2(X - \pi/4) . \qquad (8)$$

If, for example, $W(y) = y^2\lambda/4$ then $(dW/dy)^2$ is $\lambda^2/4$ at $y = 1$. Equation (8) then gives $I(5.7°)$ less than 1.3×10^{-12} at the maximum and less than 5×10^{-28} at the minimum.

c. Far-Field Effects of Phase Gratings. When the wave fronts exhibit a periodic variation, a grating effect occurs, and the crosstalk can become large for high spatial frequencies.

The far-field pattern is calculated for a circular aperture with a sinusoidal phase variation. For a phase

variation of $\lambda/4$ ($\lambda = 10.6\ \mu m$) the lowest spatial frequencies of interest are between 1.4 and 0.2 cycles/mm. The conclusion is that phase structure coarser than 0.7-5 mm in period (over a 400-mm aperture) can be ignored at large angles of observation. Structure finer than 0.7-5 mm should be treated experimentally. For a sinusoidal phase grating of amplitude P and frequency f_0, the transmission function is

$$t(x,y) = \exp\left[\frac{2\pi i}{\lambda}\,\frac{P}{2}\,\sin(2\pi f_0 x)\right]$$

$$= \sum_{\nu=-\infty}^{\infty} J_\nu\left(\frac{\pi P}{\lambda}\right)\exp(2\pi i f_0 \nu x)\ , \qquad (9)$$

which can be interpreted as a superposition of plane waves traveling in direction $\theta = \sin^{-1}(f_0\nu\lambda)$. For $P \sim \lambda/4$, we have $\pi P/X \sim 0.8$. Table IX gives values of $J_\nu(0.8)$ and $J_\nu^2(0.8)$. For $I(\theta) < \sim 1 \times 10^{-13}$ and $\theta = 6°$, we need $f_0 < 1.4$ cycles/mm. For 6×10^{-9} crosstalk, we need $f_0 < 0.2$ cycles/mm

It is thus possible to establish analytically that spatial frequencies below some limit will not cause severe crosstalk. In general, the question of higher spatial frequencies will have to be addressed experimentally for the individual optical elements involved.

d. Design Procedure with Diffraction Crosstalk. Diffraction from a circular aperture of radius r is discussed in Ref. 3. The ratio of radiation per unit solid angle relative to that in the incident beam direction can be expressed as

TABLE IX. Bessel Functions and Their Squares for Argument of 0.8

ν	$J_\nu(0.8)$	$J_\nu^2(0.8)$
0	0.85	0.7
1	0.37	0.1
2	7.6×10^{-2}	6×10^{-3}
3	1.0×10^{-2}	1×10^{-4}
4	1.0×10^{-3}	1×10^{-6}
5	8.3×10^{-5}	6×10^{-9}
6	5.6×10^{-6}	3×10^{-11}
7	3.2×10^{-7}	9×10^{-14}
8	1.6×10^{-8}	3×10^{-16}
9	7.1×10^{-10}	5×10^{-19}

$$\left(\frac{dp}{d\Omega}\right) \Big/ \left(\frac{dp}{d\Omega}\right)_i = \left[\frac{2J_1(kr\xi)}{kr\xi}\right]^2 ,$$

where

$$\xi = \left[(L - L_i)^2 + (M - M_i)^2\right]^{1/2}$$

and L, L_i and M, M_i are direction cosines in the plane of the aperture. L and M relate to the observation direction and L_i and M_i to the incident beam direction. Since the crosstalk depends only on Ω, beam locations are conveniently designated in direction cosine space. Figure 18 illustrates the use of this technique for eight multiplexed beams. A calculation performed in two rather than three dimensions can be extended to three dimensions by prudent use of the correct variables.

e. Summary. The diffraction crosstalk for a circular aperture with zero phase error is estimated by the far-field pattern and a large angle approximation. This scalar diffraction approach is valid because the maximum angle of observation is 6° and the aperture diameter is several thousand times the wavelength. For 12 orders of magnitude rejection, θ must be greater than 6°; for 9 orders of magnitude, θ must be greater than 0.6°.

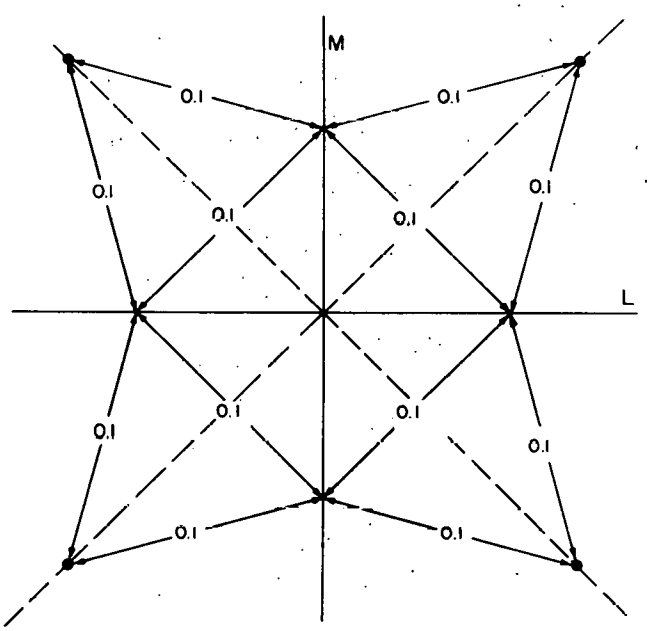

Fig. 18. A graphical representation in direction cosine space of eight multiplexed beams each separated from its neighbor by 0.1.

For small phase errors and large angles of observation, the phase errors can be neglected if their first derivative is small and higher derivatives are reasonable.

The diffraction effects of sinusoidal phase variations show that, with a $\lambda/4$ phase error, the phase error can be neglected if its spatial frequency is less than 1.4 cycles/mm (for 1×10^{-12} rejection) or 0.2 cycles/mm (for 1×10^{-9} rejection).

Crosstalk owing to higher spatial frequencies must be determined experimentally. An experimental geometry using less than the entire 400-mm diameter is possible because the spatial frequencies of interest can be sampled adequately with a smaller beam. Note also that the use of direction cosines as the diffraction variable allows a graphic solution, useful as a design tool.

The diffraction crosstalk for a multiplexed CO_2 laser system can be expressed analytically for small, slowly varying phase errors. For the conditions of validity of the expressions, the effect is indistinguishable from the perfect wave front case. For phase errors of higher spatial frequency, where an analytical solution is not feasible, an experiment must be performed.

2. **Scattering.** When a CO_2 laser is multiplexed, several beams must pass through the same gain medium. To accomplish this, those same beams must be incident on common optical elements, such as a mirror or a piece of salt. Imperfections in these materials cause high spatial frequency amplitude and phase perturbations, which divert energy from its geometric direction. This scattering phenomenon is difficult to represent analytically or to measure. The crosstalk can be expressed in terms of the usually measured scattered intensity as follows.

Consider the radiance B (W/mm^2sr). It is invariant through an optical system of transmittance 1. We wish to calculate the total power P_T on target.

$$P_T = B_T \times A_T \times \Omega_T ,$$

where B_T is radiance (W/mm^2sr), A_T is area of target (mm^2), and Ω_T is solid angle (sr) over which radiation is received.

An optical element has an intensity function I_E associated with its reflected or transmitted energy. The intensity depends in general on the difference in direction cosines between the geometric ray direction and the direction of observation and can be expressed in terms of area and radiance $I_E(L,M) = B_E(L,M)\, A_E$. Recalling that B is invariant, $B_T = B_E$ and

$$P_T = I_E \times \frac{A_T}{A_E} \times \Omega_T .$$

For a 400-mm-diam beam, a 300-μm-diam target, and an f/10 optical system,

$$P_T = 4.4 \times 10^{-9} \times I_E .$$

Scattering data from the University of Arizona are shown in Fig. 19. The quality of the data is difficult to assess. Using the data we have, for diamond-turned mirrors,

$$\frac{I_E(\theta)}{I_E(0)} = 8 \qquad \text{for } \theta \simeq 0.6°$$

and

$$\frac{I_E(\theta)}{I_E(0)} = 1 \times 10^{-3} \qquad \text{for } \theta \simeq 6° .$$

Therefore,

$$\frac{P_T(0.6°)}{P_T(0)} \simeq 3.5 \times 10^{-8}$$

and

$$\frac{P_T(6°)}{P_T(0)} \simeq 4.4 \times 10^{-12} .$$

For salt windows (Fig. 20), we have

$$\frac{I_E(\theta)}{I_E(0)} = 10 \qquad \text{for } \theta \simeq 0.6°$$

and

$$\frac{I_E(\theta)}{I_E(0)} = 2 \times 10^{-2} \qquad \text{for } \theta = 6° .$$

Therefore,

$$\frac{P_T(0.6°)}{P_T(0)} = 4.4 \times 10^{-8}$$

and

$$\frac{P_T(6°)}{P_T(0)} = 8.8 \times 10^{-11} .$$

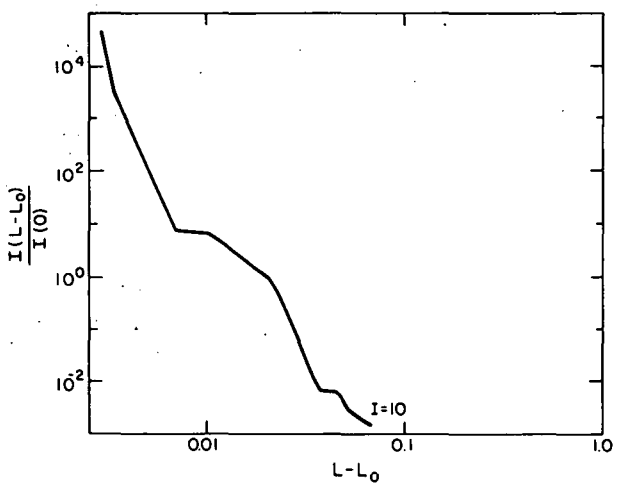

Fig. 19. Intensity of scattered radiation versus direction cosine difference of observation and incidence, for a diamond-turned mirror at 10° angle of incidence. Data are from the University of Arizona. (λ = 10.6 μm.)

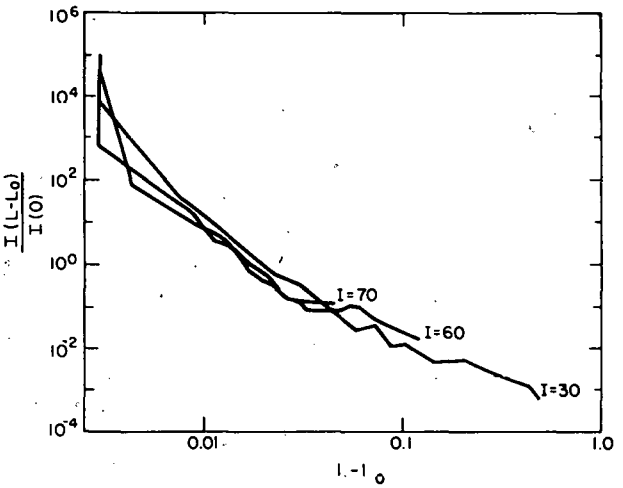

Fig. 20. Intensity of forward-scattered radiation versus direction cosine difference of observation and incidence, for a salt window at several angles of incidence. Data are from the University of Arizona. (λ = 10.6 μm.)

Scattering crosstalk must be determined experimentally. Although few data are available, a method for using such data has been shown. Use of the incomplete data shows the effects of scattering to be the same as or slightly greater than the effects of diffraction. This fact requires experiments to be performed in the future to obtain more scattering crosstalk data.

B. Focusability

The optics system for APT requires many focusing elements to put 400-kJ on target. The packaging of these beams requires larger swing radii on the Y-12 EXCELLO machine to make the necessary paraboloids and a large f-number in the target chamber. The constraints either on the alignment of the paraboloids or on the quality required for the total optical train are discussed below.

1. Off-Axis Paraboloid. A computer simulation of the optical properties of several focusing paraboloids was performed to determine the alignment requirements caused by large EXCELLO swing radii. A paraboloid was set up on the ACCOS-V optical design code. It had a vertex focal length of 96 in. and a circular aperture of 12-in. diam (f/8), which was displaced from the axis by various amounts (swing radii). The geometry is shown in Fig. 21. The incident beam was collimated with the central ray parallel to the axis of the paraboloid, the lathe axis. The image was evaluated at best focus, minimum root mean square (RMS) wave front error, for several tilt errors in the paraboloid. The results are presented in two forms: Fig. 22 plots the RMS wave front error versus tilt angle for several swing radii. The linear relationship shows that the alignment error is pure coma. Figure 23 plots the RMS wave front error versus swing radius for several tilt errors. The curves show a rather weak dependence on swing radius.

2. Component Quality. An attempt is made to estimate the quality of optical components required for APT. The approach is to scale Phase I numbers in a

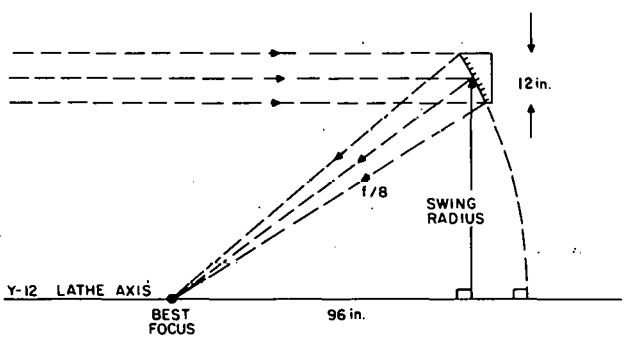

Fig. 21. Geometry for computer simulation of the effects of swing radius on paraboloid image quality.

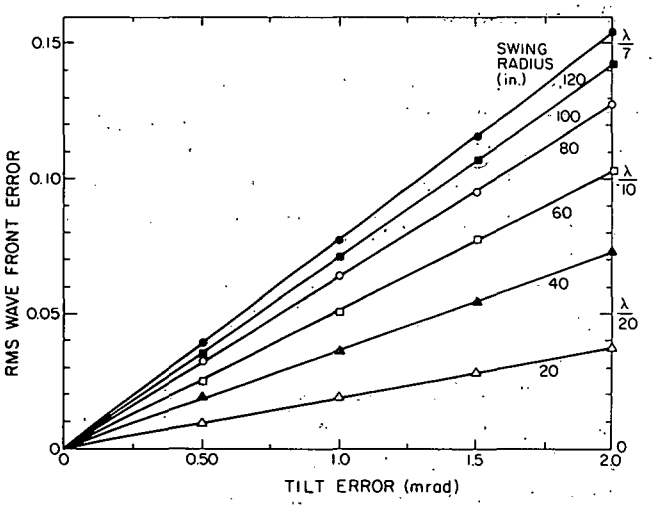

Fig. 22. RMS wave front error versus tilt error of paraboloid for several swing radii.

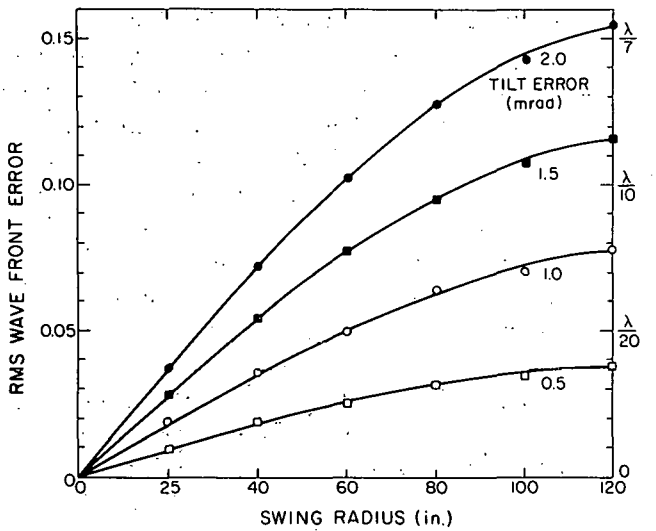

Fig. 23. RMS wave front error versus swing radius for several tilt errors.

rather sophisticated way. Consider Phase I: the specification is 80% of the energy in a diameter of 280 μm. The f-number, based on an equivalent area circle, is f/6.3. A perfect f/6.3 system would put 80% of its energy inside a diameter of 120 μm.

However, small aberrations redistribute energy from the core of the diffraction pattern to the wings. The higher the spatial frequency of the aberration, the further into the wings the energy goes. Therefore, the question can be phrased as "What quality of total system wave front error produces 80% in 280 μm?" The encircled energy will depend on RMS wave front error and a dimensionless parameter ν_0 where

$$\nu_0 = \frac{r_0}{2\lambda \text{ f-no.}} .$$

The radius of the circle into which the energy is deposited is r_0. For Antares Phase I, $\nu_0 = 1.04$. In the case of pure focus error (Figs. 24 and 25), the allowed wave front error is $\sim\lambda/7$ RMS. In the case of balanced spherical aberration (Figs. 26 and 27), the allowed wave front error is $\sim\lambda/12$ RMS.

Depending on which model is chosen to represent the wave front error of a beam line, Antares Phase I total quality must be $\lambda/12$ or $\lambda/7$ RMS. APT has a requirement of 80% in 400-μm diameter. If the optics were made to the same quality suggested by the Phase I error budget, then the f-number (F_2) required would be

$$F_2 = F_1 \frac{d_2}{d_1} = 6.3 \frac{400\ \mu m}{280\ \mu m} = 9 ,$$

where F_1 is the original f-number. However, f/9 is not feasible for APT because 168 beams require careful packaging and, therefore, more distance from the target. An f-number of ~11 seems more reasonable. An f-number of 11 requires a smaller error budget, and the cost involved would be greater.

To determine the quality required to put 80% in 400 μm for several f-numbers, we plot the RMS error required to put 80% in 400 μm versus f-number in Fig. 28. For f/11, $\lambda/10$ RMS of focus error or $\lambda/19$ RMS of balanced spherical error would be required. The better

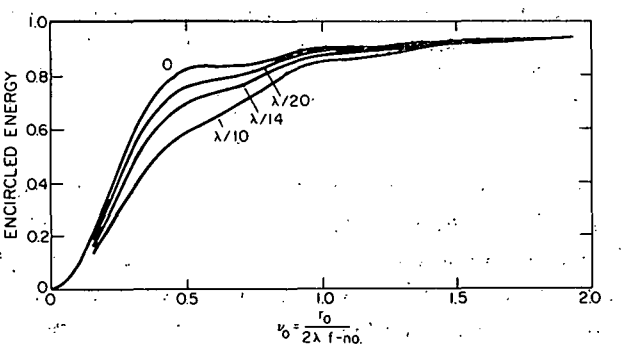

Fig. 24. Encircled energy versus ν_0 for several values of RMS wave front focus error.

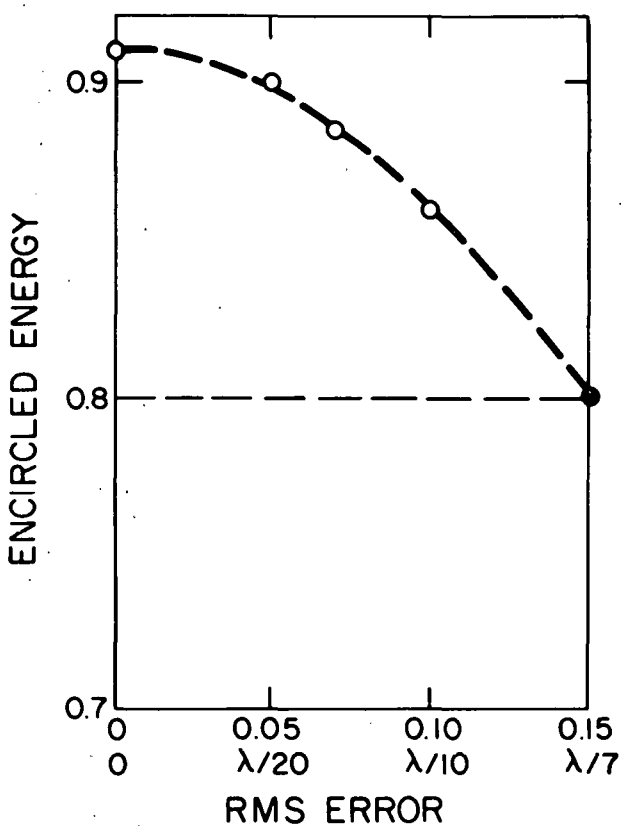

Fig. 25. Encircled energy versus RMS wave front error extrapolated from Fig. 24 for $\nu_0 = 1.04$.

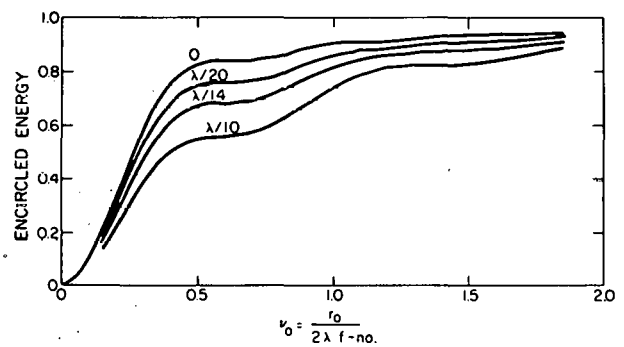

Fig. 26. Encircled energy versus ν_0 for several RMS wave front errors of balanced spherical aberration.

model to use is probably the focus error one, because most of the aberrations are astigmatic in nature. The main contributor is paraboloid misalignment. While its linear dependence on field angle indicates pure coma, it should be noted that only a small part of the total paraboloid is used, and the remaining piece of wave front is essentially astigmatic. If we use the focus model, the

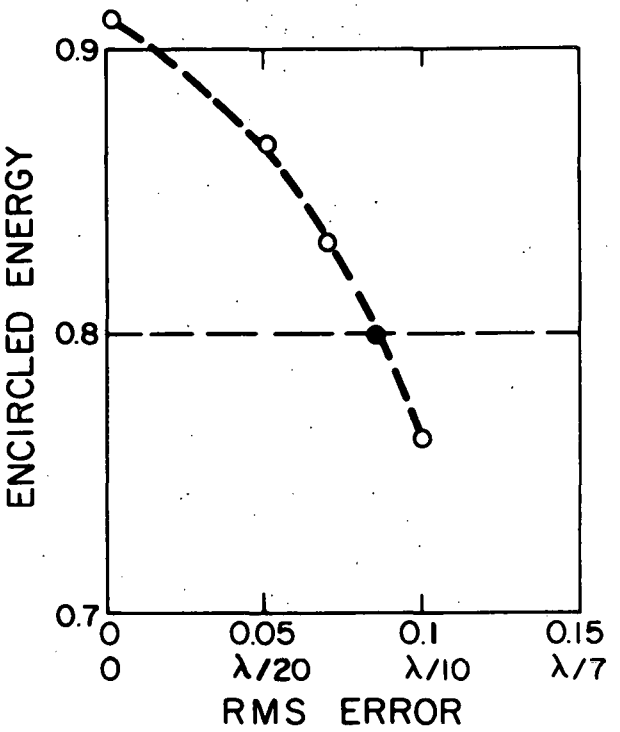

Fig. 27. Encircled energy versus RMS wave front error interpolated from Fig. 26 for $\nu_0 = 1.04$.

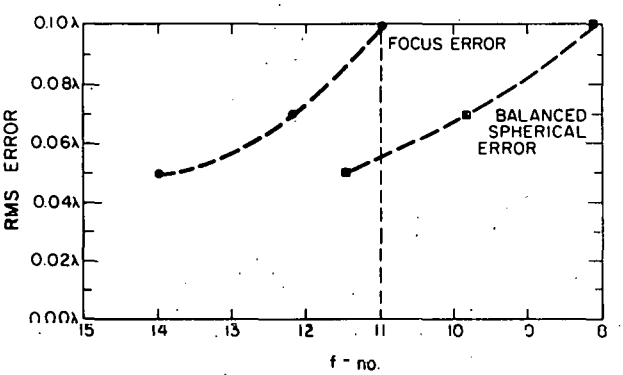

Fig. 28. Maximum RMS error for 80% of the energy to be inside 400-μm diam versus f-number.

result is λ/19 RMS, which is not difficult to obtain in view of Phase I experience.

V. OPTION DESCRIPTIONS

Three options for a 400-kJ system and five options for a 200-kJ system were studied in sufficient detail to verify

the viability of the amplifier, large-optics, and target-system designs. The options, labeled A through E, are summarized in Tables X and XI. Option C incorporates multiplexing. Rectangular packaging with amplifiers stacked vertically on each side of a two-sided E-gun was used for all options. The descriptions refer to the 400-kJ options.

Option A uses 120 amplifiers in stacks of 5 on either side of an E-gun, making 12 amplifier packages. The amplifiers would be 46 by 46 cm, and the optics arrangement would be that shown in Fig. 29, which illustrates the handling of four beams created by one tier of four amplifiers from a pair of side-by-side amplifier packages. Saturated-two-pass operation is used. Salt windows are used at each end of the amplifier. The back-reflector optic and periscope mirrors are external to the amplifier. Powered salt windows placed at the entrance to the evacuated transport tubes provide transformation of energy densities from 2.5 to 5 J/cm^2 at the target optics.

Option B incorporates amplifiers 37 by 37 cm in cross section. The amplifiers would be stacked with 7 on each side of an E-gun, creating 28 beamlets from each pair of amplifier packages. These beams would be combined into a bundle by pairs of mirrors, as for option A and as shown in Fig. 29.

TABLE X. 400-kJ Options

	Option[a]		
Amplifier Specifications	A	B	C
Discharge size (cm)	46 by 46 by 200	37 by 37 by 200	46 by 46 by 300
Multiplexing	no	no	yes
Gas mixture (N_2:CO_2)	1:4	1:4	1:2
Pressure (torr)	1800	1800	1800
Discharge current (A/cm^2)	~10	~10	~10
Discharge voltage (kV)	920	740	920
No. of amplifiers	120	168	168/4 = 42
Diam of salt windows (in.)	18	16	18
Target system options[a]	3 or 6	1, 4, or 7	1, 4, or 7
Energy storage (MJ)	17	17	12

[a]The options are described in Tables VII and VIII.

TABLE XI. 200-kJ Options

	Option[a]				
Amplifier Specifications	A/2	A/2	C/2	D	E
Discharge size (cm)	46 by 46 by 200	37 by 37 by 200	46 by 46 by 300	25 by 25 by 200	37 by 37 by 200
Multiplexing	no	no	yes	no	yes
Gas mixture (N_2:CO_2)	1:4	1:4	1:2	1:4	1:2
Pressure (torr)	1800	1800	1800	1800	1800
Discharge current (A/cm^2)	~10	~10	~10	~10	~10
Discharge voltage (kV)	920	740	920	500	740
No. of amplifiers	60	84	84/4 = 21	168	168/4 = 42
Diam of salt windows (in.)	18	16	18	12	14
Target system options[a]	2, 3, 5, or 6	all	all	1, 3, or 7	1, 4, or 7
Energy storage (MJ)	8.7	8.7	6	8.7	6

[a]The options are described in Tables VII and VIII.

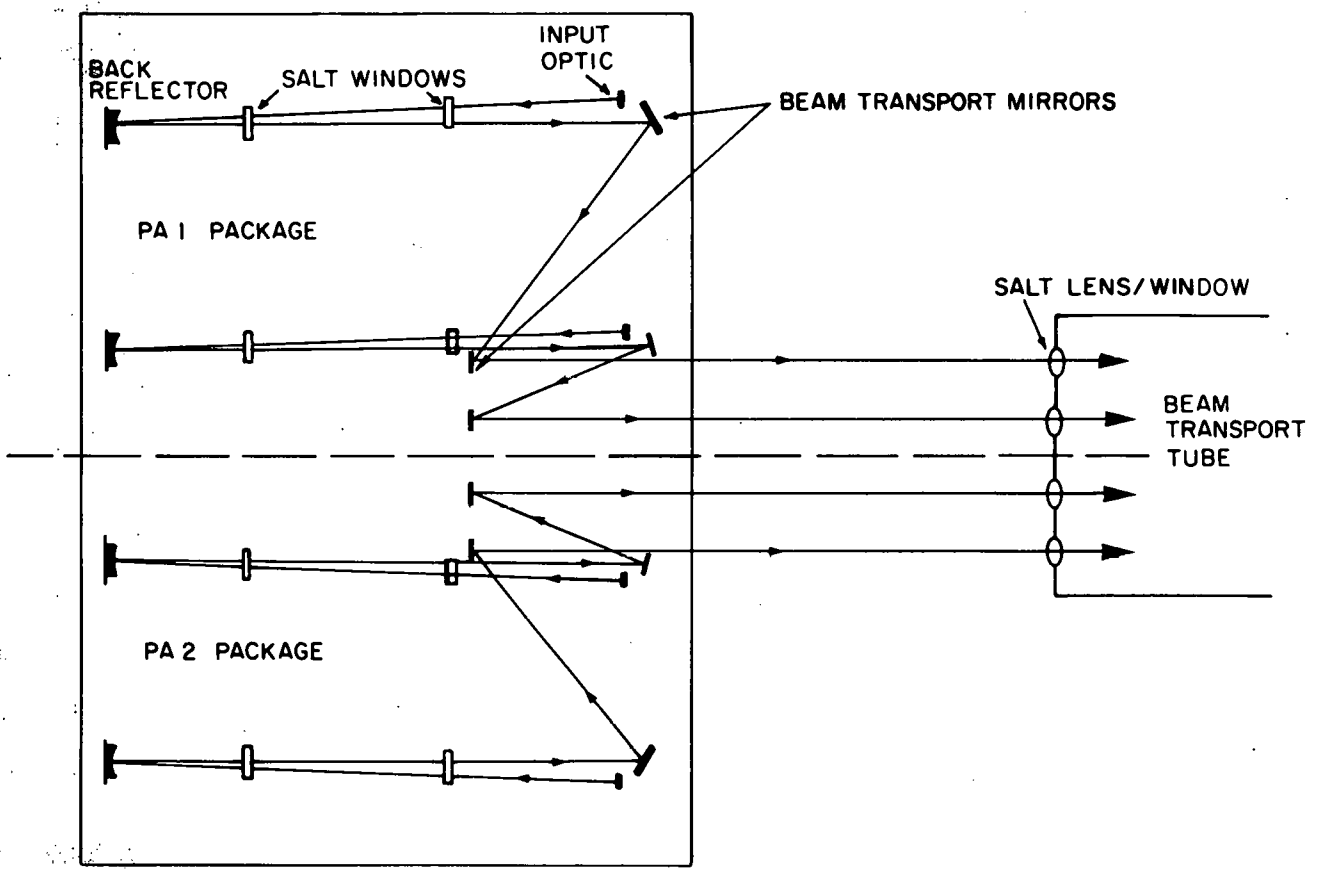

Fig. 29. Optics layout of a Power Amplifier pair. Twenty-eight beams are produced, bundled, and directed into a beam tube by sets of transport mirrors. Four beams from one of seven tiers of amplifiers are shown, with the beam starting at the input mirror and following the two-pass route.

The arrangement of 12 amplifier packages in the present Laser Hall, shown in Fig. 30, could accommodate either nonmultiplexed option, A or B. The outlines are to scale and include the space necessary for optics, power cables, etc. Energy supplies for the E-gun are not included; they would have to be located elsewhere. The 90-ft depth includes the aisle now present behind Antares I amplifiers. Removal of the back-reflector complex from amplifier packages 1, 2, 5, 6, 9, and 10 would be required to reopen this corridor. The space south of the aisle, now allocated for energy supplies and not shown in the illustration, remains available but probably will be inadequate to house all energy supplies needed for these options. Additional space to the west of the present building is available.

For the multiplexed (four-plexed) Option C, 6 packages of 14 amplifiers are grouped in pairs (Fig. 31). The amplifier optics in this case did not use a salt window on the side facing the back reflector because the 2° angle between beamlets required too large a window. The 168 beamlets exit the Laser Hall in a westerly direction, and 12 mirror stations redirect and introduce required delays in the beamlets. The beamlets ultimately enter the target building in 6 bundles of 28 beamlets each. A powered salt window is used at the entrance point to the target building to avoid the necessity of maintaining a vacuum in the beam transport-mirror station complex. However, a controlled atmosphere for this complex must be provided. The required beam delay is provided by multiple traverses between stations C and D, as illustrated in Fig. 32 for a group of four beamlets arising from one amplifier in package No. 1.

As noted in Tables X and XI the five 200-kJ options use four amplifier cross-section sizes, which span the range set by the limitations described in Sec. II. Three of the five options are halved 400-kJ designs. The other two use small amplifiers.

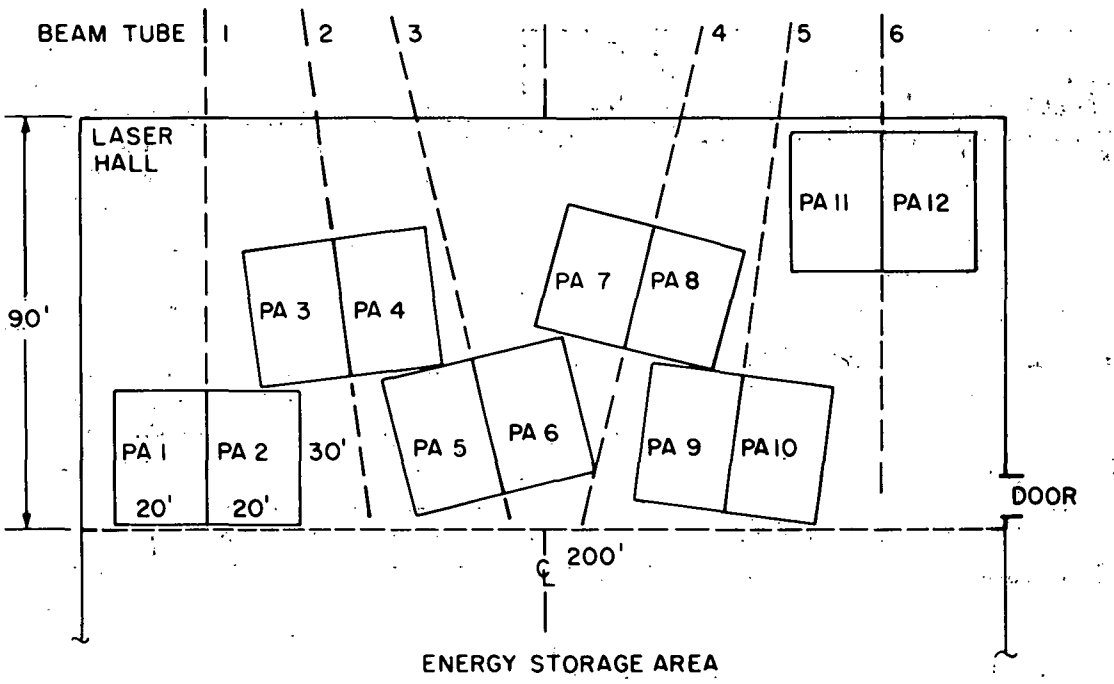

Fig. 30. Layout of 400-kJ amplifier system in the existing Laser Hall. The outlines encompass all space needed for external optics, cable connectors, etc.

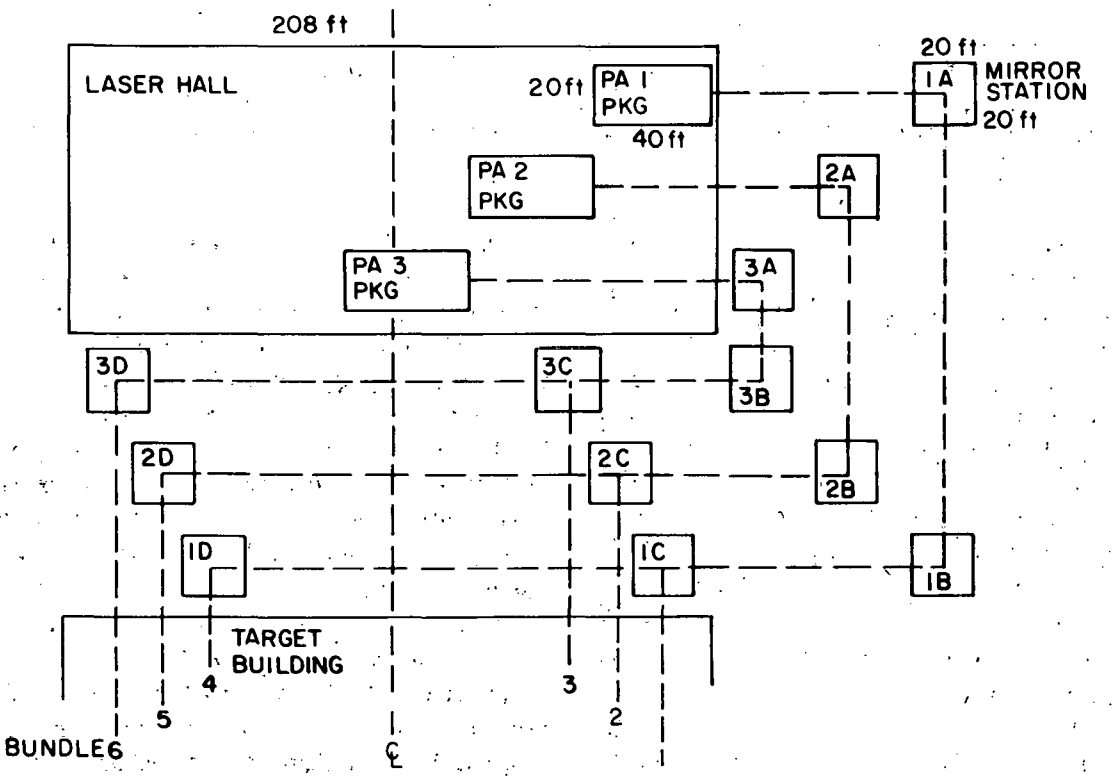

Fig. 31. Layout of a four-plexing 400-kJ system. Fifty-six beams emerge from each of three amplifier packages and are sent to turning chambers located west of the Laser Hall and thence to delay lines and turning mirrors, which redirect them into the six beam tubes.

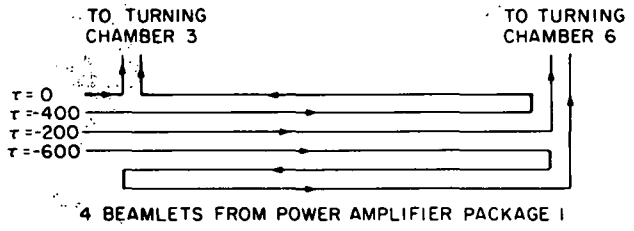

Fig. 32. Illustration of a delay line scheme. Fifty-six beams from an amplifier package arrive at the delay line complex at four different times. Four different path lengths are used to make the beams simultaneous before they are redirected into a pair of beam tubes.

The seven target system designs are described in Sec. III, and the possible combinations with the 200- and 400-kJ amplifier systems are noted. All the options are based on 1800-torr operation. This should not be construed to imply recommendation of this pressure; rather it is an attempt to put all options on an equal footing with respect to this parameter.

No options using guide magnetic fields have been explored. Unless larger windows are contemplated, the improvement in unformity would not warrent the additional cost and complexity.

VI. COST ANALYSIS

A. Basis for Cost Figures in Preliminary APT Review

1. **Source of Information.** The cost figures for the options considered were obtained from the following sources.

- Cost to-complete estimate for each element of the Antares I program was obtained from each subsystem project manager of Antares I. All details that made up the cost were reviewed so that applicable costs could be used for APT.
- Estimates of fabrication costs were made using present shop rates, along with assistance from L-10, CMB-6, and SD personnel in their fields of expertise.
- Catalogue prices were used, and vendors of raw materials were contacted for significant standard cost items.

2. **Costs by Project Area.**

a. Controls. Controls costs for Antares I were reviewed with Michael Thuot. The present system was considered available for APT. The costs were separated into fixed costs and costs per beam line. Depending on the number of beam lines, an additional central computer would be required, and it is included in the costs. These costs should be fairly accurate since Thuot has a very detailed breakdown of his system costs along with latest prices, and a breakdown of manpower needed to implement the system. The increment cost is \$60k per beamlet. An additional computer adds \$1500k. For the larger system \$3000k to \$5500k worth of additional design and software development is expected.

b. Power Supplies. Costs in this area were reviewed with Garry Allen, who has an excellent set of records on his total costs for the Antares I power requirements. It was decided to calculate an overall cost per joule of stored energy and then to use this number for the power requirements of the various systems. The cost is very near \$1.00/J for material and installation labor.

c. Large Optics for Amplifier. Again, very detailed costs on salt windows, copper mirrors, holders, etc., were kept by Messrs. Reichelt and Munroe. We established curves for costs of all these components and used the curves to establish costs for APT. Table XII shows costs of large optics by amplifier option. The options labeled A through E are those described in Tables X and XI. Note that this category includes only the optics associated with the amplifier and entry into the beam tube.

d. Amplifiers. Robert Stine reviewed the costs from his records on the Power Amplifier modules. The costs of several elements were used directly as they probably would not change significantly in APT. These elements were the cable terminations, gas and vacuum system, diagnostics, interconnecting cables, and electrical-optical check-out.

The amplifier shells were laid out for each configuration and weights of the assemblies were determined. An average cost of \$5.00/lb was obtained, using the following factors.

- Analysis of the various shells of the Antares I system gave an average cost of \$5.00/lb.
- The driver amplifier shell cost from the Systems, Science and Software quotation was on the order of \$4.00/lb. Configuration for the individual beamlet modules is almost identical to that contemplated for APT, although somewhat smaller.
- The amplifier configuration cost was estimated by SD personnel. By consensus, a total 3000-4000 hours of

TABLE XII. Cost Estimate Per Beamlet-Large Amplifier Optics (k$)

	Option				
	A	B	C	D	E
Amp. windows					
Flat salts	50	32	25	14	16
Holders	17	12	28	11	26
Powered salt	28	18	72	9	36
Coating	15	15	25	10	17
Subtotal	110	77	150	44	95
Large mirrors					
Mirrors	9	9	51	9	51
Mounts	24	24	142	15	91
Subtotal	33	33	193	24	142
Small mirrors					
Mirrors	5	5	40	5	40
Fixed mounts	1	1	8	1	8
Motorized mounts	3	3	20	3	20
Subtotal	9	9	68	9	68
Total/amplifier	152	119	411	77	305
No. of amplifiers	120	168	42	168	42
Grand total	18 240	19 992	17 262	12 936	12 810

labor was used for the assembly under consideration. This cost was under $5.00/lb. Material and labor costs for the balance of the parts to make up the Power Amplifiers were estimated by the appropriate personnel.

Costs for the two packaging schemes (circular and rectangular) were compared. The results are shown in Table XIII. The costs are for a package of eight amplifiers as shown in Figs. 6 and 7. The overall costs are slightly lower for the circular packaging. The final option selection, however, uses rectangular packaging to allow 14 amplifiers per package instead of 8, the maximum allowed for circular packaging.

e. Optical System. The total costs for the Antares I system were determined per beamlet. These were then projected to APT, dependent on the number of beams for the projected system. An incremental cost of $80k per beamlet was used.

f. Front End. If triple-pass designs are used, costs over and above present front-end equipment should be moderate ($500k). A 10-kJ driver system adds $2900k.

g. Target System. Vernon Ziegner reviewed costs for the target chamber, turning chambers, and optics for Antares I. Optics figures were projected to the seven options given for APT. No cost estimates for vacuum system alterations were made. The breakdown of costs for the seven options is given in Table XIV.

h. Design Labor. These estimates are based on responses of the Antares I program managers to the question, "If we were required to design a new system for

TABLE XIII. Amplifier Costs (Fabrication and Materials). Comparison for Rectangular and Circular Packages of Eight Amplifiers (k$)

	Rectangular		Circular	
	12 in.	18 in.	12 in.	18 in.
Chamber	346	546	170	349
Plast. div.	52.3	87.5	58.8	107.6
Hibachi sec.	42.9	54.6	42.9	54.6
Salt windows	220	488	220	488
Support	15	25	15	25
Cable term.	160	212.5	160	212.5
HV cables	60	120	60	120
E-guns	84	114.5	77	99
Anodes	9.6	13.6	9.6	13.6
Gas and vacuum systems	375	375	375	375
Assembly	25	35	25	35
Totals	1 390	2 072	1 213	1 879

TABLE XIV. Cost Estimate-APT Target System Options (k$)

	1	2	3	4	5	6	7
Mirrors	2 300	1 000	1 500	3 100	1 300	2 100	2 300
Mirror positioners	3 000	1 300	2 100	4 200	1 800	2 900	3 000
Mirror positioner wedges	170	170	120	340	140	230	170
Turn mirror supp. plates	190	140	160	190	140	160	190
Turn mirror supp. stands	180	140	160	180	140	160	180
Fold mirror supp. plates	190	140	160	190	140	160	190
Focus mirror supp. plates	190	140	160	190	140	160	190
Spacer frame	500	500	500	500	500	500	500
Handling fixtures	200	200	200	200	200	200	200
Salt windows	2 700	1 200	1 800	3 900	1 700	2 600	3 900
Salt window frames	500	200	340	500	200	340	500
Salt window shipping cont	90	40	60	90	40	60	90
Totals	10 210	5 170	7 260	13 580	6 440	9 570	11 410

APT using our present knowledge and possible carry-over from Antares I, how many man-hours would be required to document the system with working drawings?" The results, in man-years, are summarized in Table XV. Half the man-years are for staff members and half for designer-technicians.

i. Handling Equipment. During our evaluations, it was pointed out that handling-equipment (cranes, etc.) costs on Antares I are projected to be ~2% of the total Antares I cost. These costs are not detailed, but they are lumped into the various subsystem estimates.

TABLE XV. Design Costs for Any APT Option

	Man-Years
Large optics	3
Front end	24
Power amplifier	90
Energy storage	20
Controls	6
Optical system	45
Target system	40
Total	228

B. Option Costs

Cost estimates for 200-kJ and 400-kJ options are given in Tables XVI and XVII. The estimates result in a range of costs depending on selection of target system option and front-end requirements. Estimated completion costs to build the full six-amplifier Antares I are shown in Table XVIII. As detailed in Sec. VI. A, the estimates are based on established information, and they are carried out to a level of detail commensurate with that used in defining the options. The analysis is intended to aid in the process of option selection. Ultimate project cost estimates would need to include costs for design, development, prototyping, etc. If these costs are ignored, we see that the cost per joule of output for the proposed options is substantially less than for the completion of Antares. Several factors are responsible for the difference.

- Beamlet energies are higher: as much as 3.5 kJ versus 1.7 kJ for Antares, and the costs of many items are proportional to the number of beamlets.
- Optics energy loadings are higher: 2.5 J/cm^2 versus <2 J/cm^2 for salt and 5 versus <3 J/cm^2 for copper mirrors in Antares. Optics costs per joule are thus substantially less.
- Amplifier costs have been reduced greatly by increasing efficiency and decreasing the size. Exclusive of all optics, but including assembly labor, the new amplifier options are estimated at \$76/J versus \$215/J for Antares.
- Energy storage requirements per joule are substantially less because of improved amplifier performance.

VII. ANTARES I STUDY

A recent study[4] of Antares upgrade possibilities led to the conclusion that the Antares power-amplifier module (PAM) could produce 20 kJ in a nanosecond. Because completion of the original six-amplifier Antares system is an option that should be considered, a more detailed analysis of the expected performance of Antares I was conducted as part of our option survey. The analysis was limited to more detailed calculations (including nonuniformities) of the electrical discharge and energy extraction. Performance was calculated with one- or four-line operation, with and without a saturable absorber between the first and second amplifier passes. A calculation also was made with a reshaped "uniform" discharge. The results of the calculations support the expectation of 20-kJ output from the PAM. The improved performance results simply from using the energy supplies at full rated capacity as opposed to the more conservative mode contemplated for the 16.67-kJ original amplifier performance specification. Operation at 1800 torr of 1:4 (N_2:CO_2) mix was used. Use of higher operating pressures could alleviate parasitic oscillations, but a careful re-examination of pressure-vessel integrity would be required. The analysis proceeded in several steps as discussed below.

A. Coupling of Energy into the Discharge

The energy storage system and transfer system were represented by an L-C Marx and six coax cables as illustrated in Fig. 33. The discharge was represented as a recombination-limited variety with the drift velocity and recombination coefficient dependent on E/N. The time evolution of the discharge was such that the election density generally did not assume its equilibrium value. The ionization source was assumed constant for lack of better information; its magnitude was adjusted to give the desired level of peak current density. The electric field is taken to be the discharge voltage divided by the anode-to-cathode spacing. The resulting waveforms for current and electric field are shown in Fig. 34. The shape of these curves is influenced by the nonlinear character of the discharge and the cable transit times. At early times, the discharge impedance exceeds the characteristic impedance both of the cable and of the Marx Generator.

TABLE XVI. 400-kJ Cost Analysis (k$)

	Option		
	A	B	C
Amplifier			
Units	24 240	23 688	13 482
Optics	18 180	19 908	17 262
Labor	7 000	8 400	8 400
Stands	1 000	1 000	1 000
Target system cost range[a]			
Hardware and labor	7 260-9 570	10 200-13 580	10 200-13 580
Controls			
Hardware and software	11 260	14 140	11 940
Energy supplies			
Equipment and labor	17 140	17 140	12 000
Optical system			
Equipment and Labor	9 600	13 440	13 440
Front-end cost range[b]	500-2 900	500-2 900	500-2 900
Building modifications	2 000	2 000	2 000
Totals	98 180-102 890	110 416-116 196	90 224-96 004

[a]The range reflects the availability of several options.
[b]The range shows the dependence of the front end on total drive required.

TABLE XVII. 200-kJ Cost Analysis (k$)

	Option				
	A/2	B/2	C/2	D	E
Amplifier					
Units	12 120	11 844	6 741	21 336	8 883
Optics	9 090	9 954	8 631	12 852	12 768
Stands	500	500	500	700	700
Target system cost range[a]					
Hardware and labor	3 630-6 440	5 100-6 790	5 100-6 790	10 200-13 580	10 200-13 580
Controls					
Hardware and software	5 630	7 070	5 970	14 140	11 940
Energy supplies					
Equipment and labor	8 570	8 570	6 000	8 570	6 000
Optical system					
Equipment and labor	4 800	6 700	6 700	13 400	13 400
Front-end cost range[b]	500-1 450	500-1 450	500-1 450	500-1 450	500-1 450
Building modifications	2 000	2 000	2 000	2 000	2 000
Totals	46 840-50 600	52 238-54 878	42 142-44 782	83 698-88 028	66 391-70 721

[a]The range reflects the availability of several options.
[b]The range shows the dependence of the front end on total drive required.

TABLE XVIII. Completion of Antares I Cost Analysis (k$)

Amplifier	
Units	11 828
Optics	4 600
Labor	4 968
Stands	400
Target system	
Hardware and labor	3 314
Controls	
Hardware and software	3 115
Energy supplies	
Equipment and labor	4 050
Optical system	
Equipment and labor	9 641
Front end	2 900
Building modifications	0
Total	44 816

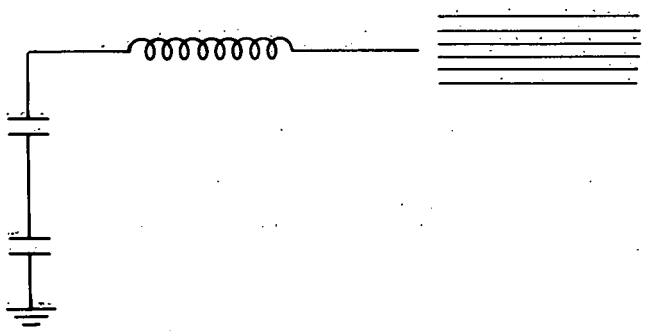

Fig. 33. Circuit for Antares-like Marx energy supplies. There are six cables at 36 Ω each with a 150-ns transit time. The capacitor is 2.8 μF, and there are 20 stages giving a total capacitance of 0.42 μF. The rated voltage is 60 kV per stage, 1200 kV total.

B. Distribution of E and j in the Discharge

E and j vary throughout the discharge because the primary ionization varies and the discharge is not rectangular. A Monte Carlo type calculation is used to predict the spatial dependence of primary ionization under assumed electric and magnetic fields along with the specified character of the primary electron beam impinging on the entrance foil. With the ionization distribution as input, current and voltage distributions

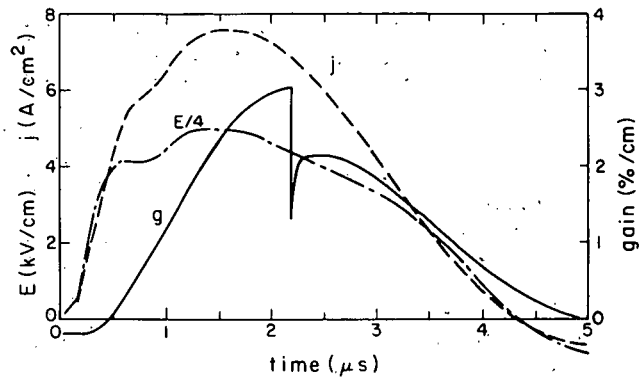

Fig. 34. Time history of current density, electric field, and gain for an Antares-like discharge. Energy is extracted at maximum gain, 2.2 μs.

are calculated. A recombination-limited discharge is assumed (electron density equal to the square root of the ratio of ionization rate to recombination coefficient). The dependence of drift velocity and recombination coefficient on E/N is included. A two-dimensional solution is obtained by an iterative algorithm to obtain a self-consistent result appropriate for the electrode and discharge geometries. The Antares discharge is 75 cm long and has a cross section as illustrated in Fig. 35. The discharge is confined by plastic dividers on the sides. Symmetry about the center line was assumed. Calculations were performed with a 15 by 7 mesh and the results for E (kV/cm with 500 kV across electrode), relative j, and relative power are given in Fig. 36. Table XIX lists

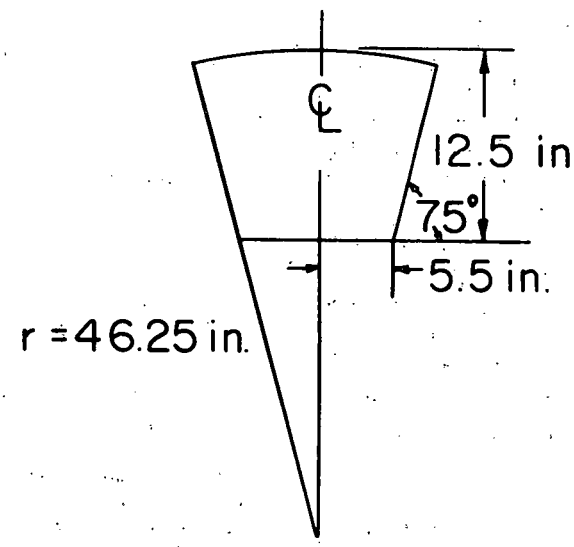

Fig. 35. Cross section of the Antares discharge.

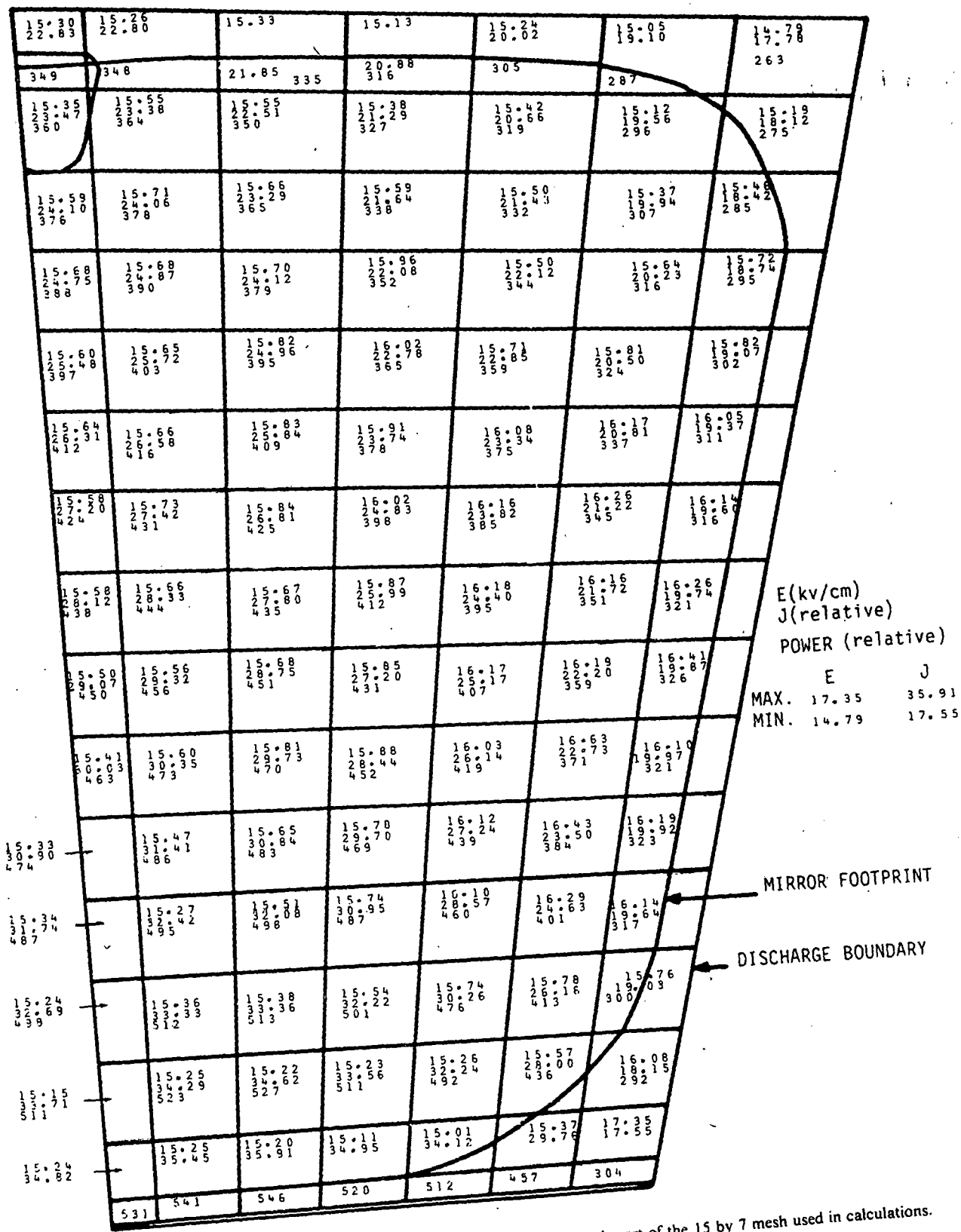

Fig. 36. Electric field, relative current density, and relative power for each part of the 15 by 7 mesh used in calculations.

TABLE XIX. Relative Values of Reciprocal Square Root of Primary Ionization

			Cathode				
	1.065	1.047	1.028	1.047	1.059	1.255	2.597
	1.089	1.083	1.070	1.104	1.153	1.375	2.200
	1.135	1.127	1.129	1.191	1.296	1.506	2.035
	1.182	1.148	1.191	1.266	1.427	1.687	2.068
	1.213	1.211	1.258	1.326	1.500	1.777	2.057
	1.259	1.271	1.328	1.400	1.547	1.835	2.036
Center	1.312	1.310	1.354	1.458	1.632	1.854	2.115
Line	1.369	1.372	1.398	1.530	1.685	1.888	2.097
	1.415	1.427	1.477	1.628	1.723	1.953	2.088
	1.474	1.462	1.531	1.682	1.742	1.973	2.093
	1.515	1.509	1.583	1.773	1.709	1.927	2.075
	1.574	1.566	1.618	1.817	1.719	1.915	2.087
	1.600	1.624	1.668	1.781	1.780	1.888	2.064
	1.601	1.642	1.705	1.769	1.831	1.871	2.039
	1.636	1.632	1.715	1.754	1.851	1.902	1.975
			Anode				

relative values of the reciprocal square root of primary ionization as used for the calculations. It assumes 500-keV primary electrons and a 500-keV discharge. The discharge volume accessed by the outgoing laser beam was subdivided into 20 subareas of moderately constant power deposition. These are shown in Fig. 37 with average values of E and j; which have been normalized to reflect maximum voltages and current. For this case, $\bar{P}/P_{max}$ is 0.77. Small signal gain was calculated for each of the 20 subareas. The values at 2.2 μs are displayed in Fig. 38. The values are strictly appropriate for the amplifier when no magnetic fields are present. At the ends where magnetic fields force the primary electrons toward the center, the gain values will be lower and a somewhat different distribution occurs. By the same token, the actual gains in the central regions will be higher. Because the extraction direction integrates over the major variation caused by the magnetic field, the calculated total energy is insensitive to this nonuniformity. The end-to-end nonuniformity was not included in this study.

Energy extraction calculations were made using Frantz-Nodvik formulations[5] with effective available energies for 1-ns pulses. Checks were made of selected cases using the more sophisticated formulation developed by Feldman.[6] Figure 39 illustrates the longitudinal geometry. The first pass is an expanding pass and was so treated. The variation in gain over the cross

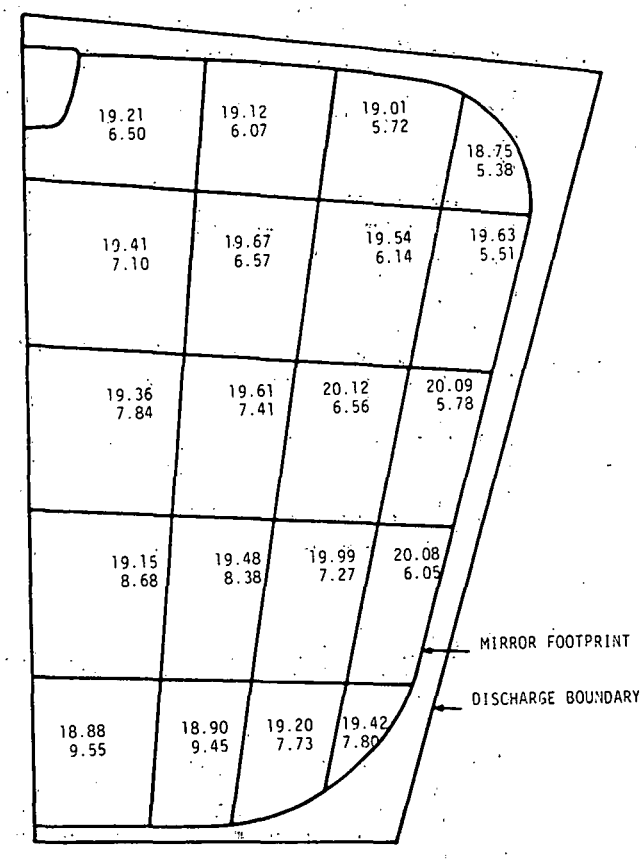

Fig. 37. Area in centimeters squared and relative power deposition for each subdivision of the laser beam.

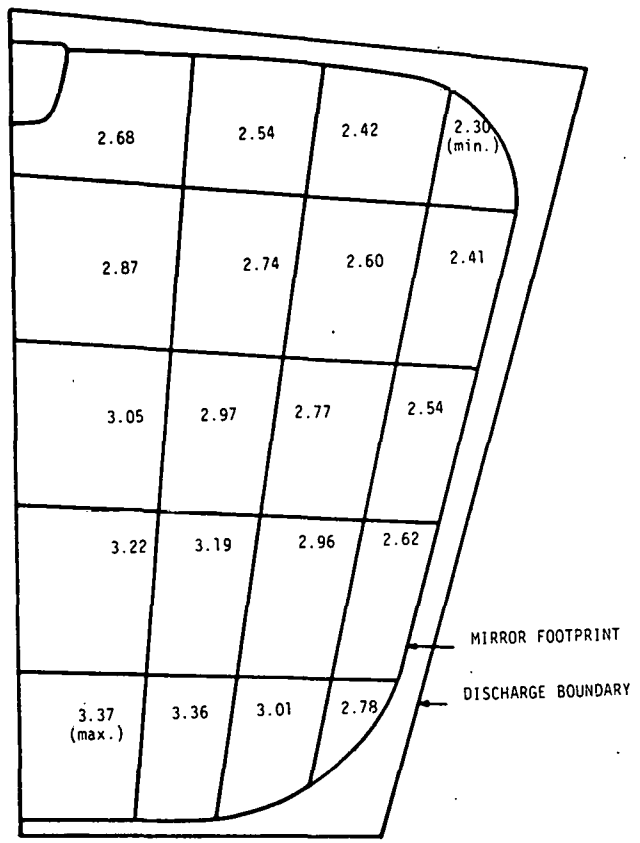

Fig. 38. Small signal gain at 2.2 μs within each subarea.

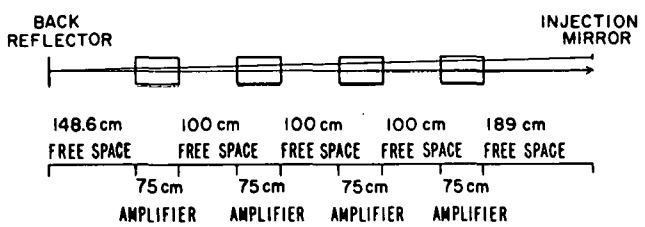

Fig. 39. The longitudinal geometry of the two-pass Antares beam path. Four gain regions are interspersed with unpumped laser gas, labeled as free space.

section was accounted for. Integration was performed along the path of the central ray of each of the 20 subareas. The input energy density for each subarea was as prescribed in Fig. 40. Figure 41 illustrates the behavior on the expanding pass. The final output pass is calculated by application of the Frantz-Nodvik formulation with the results of the first pass as input. Output energies for single-line and four-line cases are shown in Figs. 42 and 43.

The case with a saturable absorber is shown in Fig. 44. A Helios-like absorber was assumed (two-pass large-signal transmission of 0.5). Table XX summarizes the results of the study.

Because significant energy extraction occurs near the end of the first pass, its effect on second-pass performance must be considered. For Antares the effect amounts to a reduction of the second-pass energy contribution by one-half of the first-pass energy contribution.

The output values quoted in Table XX were reduced by 3% to account for volume utilization losses (slightly converging beam) and by 8% reflection losses at the exit salt window. As noted earlier, an expectation of 20 kJ out is verified, but it should also be noted that the window loading has values as high as 2.8 J/cm^2. The Antares beam cross section was chosen to maximize area but, in turn, forced a very nonuniform distribution.

The question of whether a smaller area with more uniform beam might be preferable was addressed by examining such a case. The results are shown in Figs. 45-48. The total output is virtually unchanged, the beam is considerably more uniform, but the peak window loading reaches 2.9 J/cm^2 and, of course, the average loading is much higher also.

The adequacy of the Frantz-Nodvik energy extraction with an effective available energy also was examined in a few cases by comparing it with the Feldman formulation. The results are shown in Table XXI.

POSTSCRIPT

The interim APT report was prepared in October 1980 as a summary of 3 months of effort devoted to the first part of a planned two-part effort that would lead to an Antares upgrade design. Changing perspectives and program plans eliminated the need to proceed immediately with the rest of the program. However, interest in advanced CO_2 laser facilities persists, and the desirability of issuing the interim report in a more formal fashion became apparent. This report is the result. The organization of the interim report was revised, and a small amount of additional exposition was added to improve clarity and communication with the reader. No data or numerical information has been changed, and the reader should be aware that costs correspond to FY 80 values.

Current discussion of future CO_2 lasers frequently includes requirements significantly different than those

imposed in this search for design options. Most significant are the consideration of longer pulses (10 ns), larger spot sizes, and more allowed prepulse energy. The longer pulse has major impact on the target system design. The shorter pulse effectively limited APT designs to 400 kJ. With the increase in mirror loading permitted by the longer pulse, megajoule designs that fit into the target building can be devised. On a per-joule basis, the amplifier design is also easier.

0	0	0	0	0	0	0	0	0	0	0	0	0	0	0	0	0	0	0	0	0
0	0	0	0	0	0	0	0	1	1	1	1	1	0	0	0	0	0	0	0	0
0	0	1	2	2	3	4	5	5	6	6	6	5	5	4	3	2	2	1	0	0
0	3	5	6	9	12	15	18	20	21	22	21	20	17	15	12	9	6	5	3	0
0	2	6	9	13	17	22	26	29	31	32	31	29	26	22	17	13	9	6	2	0
0	3	10	13	20	27	34	41	47	50	51	50	46	41	34	27	20	13	10	3	0
0	5	14	16	26	35	45	54	62	67	69	67	62	54	45	35	26	16	14	5	0
0	2	15	22	31	43	55	68	77	84	86	84	77	67	55	43	30	22	14	2	0
0	3	9	24	33	47	61	75	86	94	96	94	86	75	61	47	33	24	9	3	0
0	2	9	28	32	49	62	78	89	98	*	97	89	77	62	48	31	28	9	2	0
0	0	4	22	32	43	59	72	84	91	94	91	84	71	58	43	31	22	4	0	0
0	0	4	10	28	37	50	62	73	80	82	80	73	62	50	36	28	10	4	0	0
0	0	1	7	23	27	39	48	57	62	65	62	57	48	39	27	23	7	1	0	0
0	0	0	6	16	18	28	35	42	46	48	46	42	35	28	18	16	6	0	0	0
0	0	0	1	9	13	16	22	25	29	29	29	26	22	16	13	9	1	0	0	0
0	0	0	1	1	7	11	14	17	19	20	19	18	14	11	7	1	1	0	0	0
0	0	0	0	0	1	3	4	5	5	6	5	5	4	3	1	0	0	0	0	0
0	0	0	0	0	0	0	0	0	1	1	1	0	0	0	0	0	0	0	0	0
0	0	0	0	0	0	0	0	0	0	0	0	0	0	0	0	0	0	0	0	0

MAX INTENSITY (100 RELATIVE=*) IS 1.04628 J/CM2

TOTAL ENERGY=3.37584 JOULES

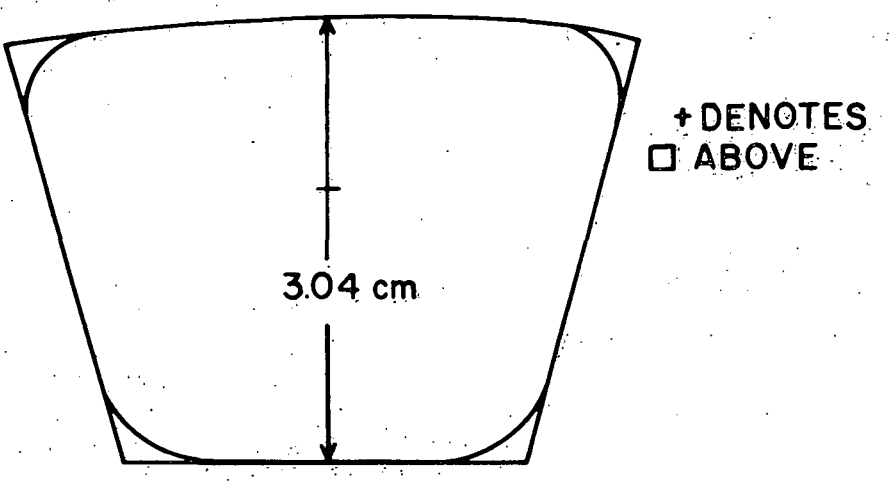

Fig. 40. The footprint of the Antares beam at an injection mirror and the relative energy of the beam throughout the mirror.

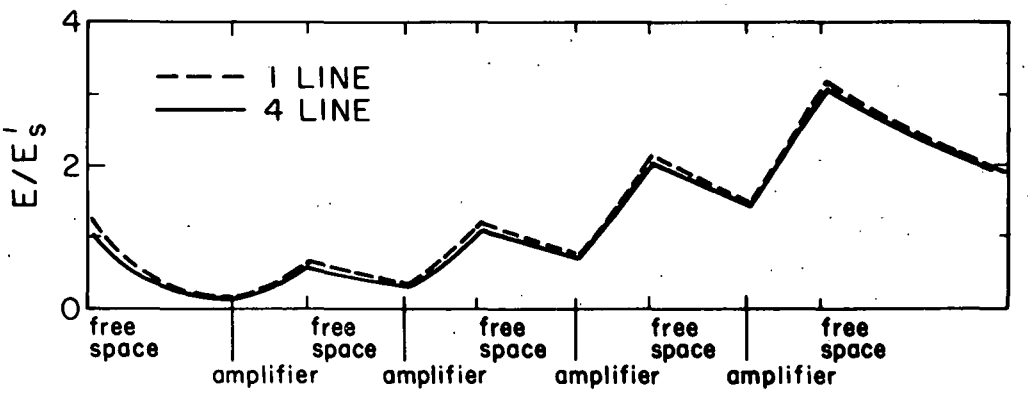

Fig. 41. Energy density versus position on the expanding pass in Antares. The fall in energy density between amplifiers and at the ends results from the expanding character of the beam as well as from absorption.

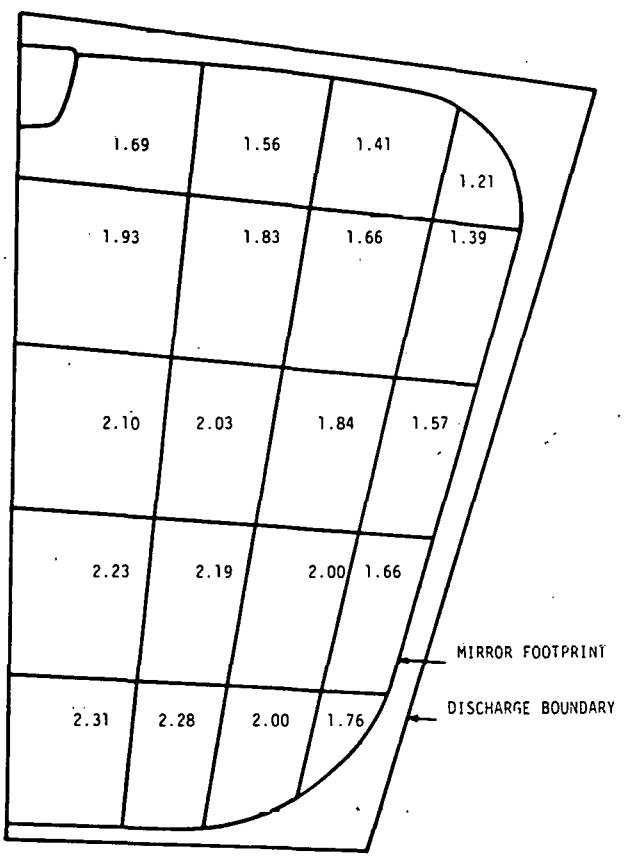

Fig. 42. Half the beam footprint at the back reflector divided into subareas with E(out) for one-line extraction shown in each subarea.

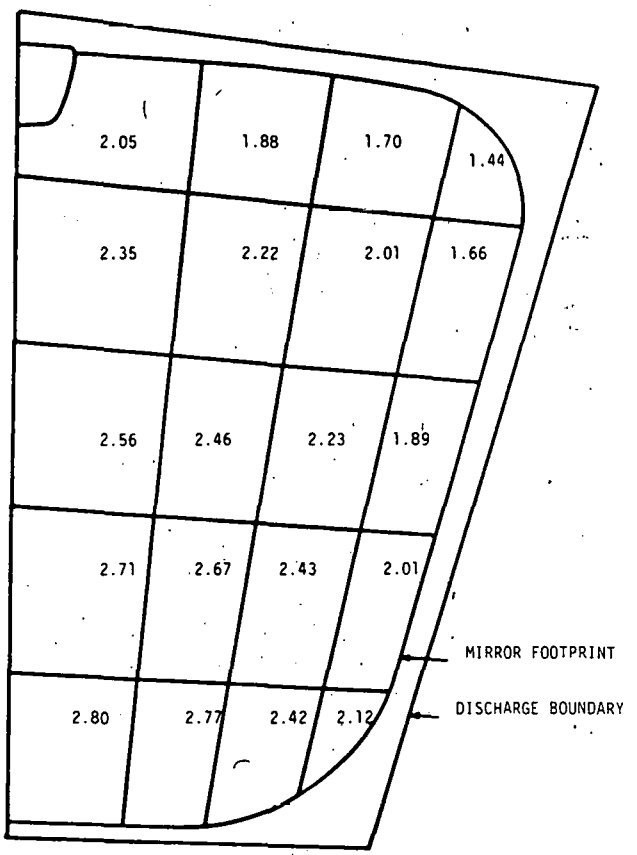

Fig. 43. Half the beam footprint at the back reflector divided into subareas with E(out) for four-line extraction shown in each subarea.

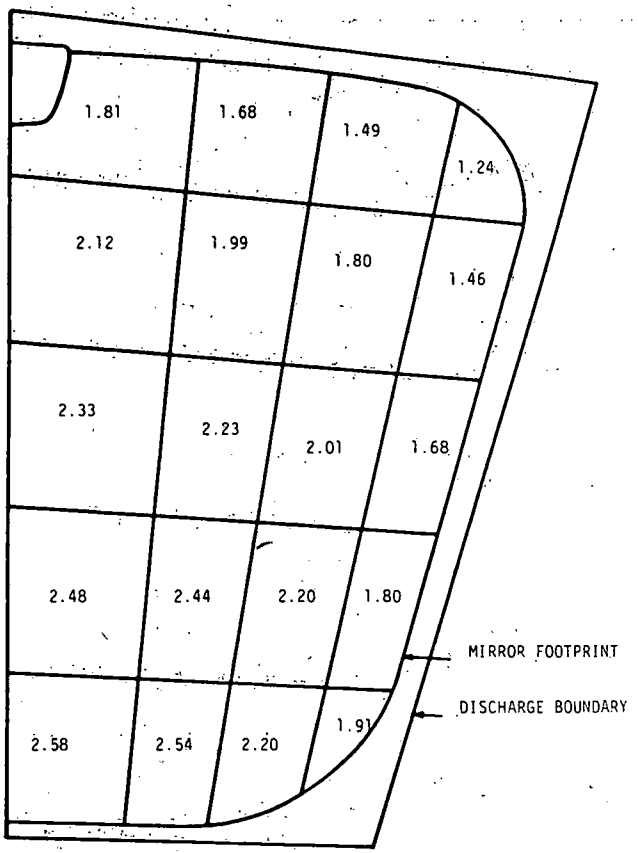

Fig. 44. Half the beam footprint at the back reflector divided into subareas with E(out) for four-line extraction with a saturable absorber.

TABLE XX. Performance of Antares I

	Output (kJ)	
	One Line	Four Lines
No saturable absorber	19.5	23.6
With saturable absorber		21.4
Output from first pass	2.1	2.4

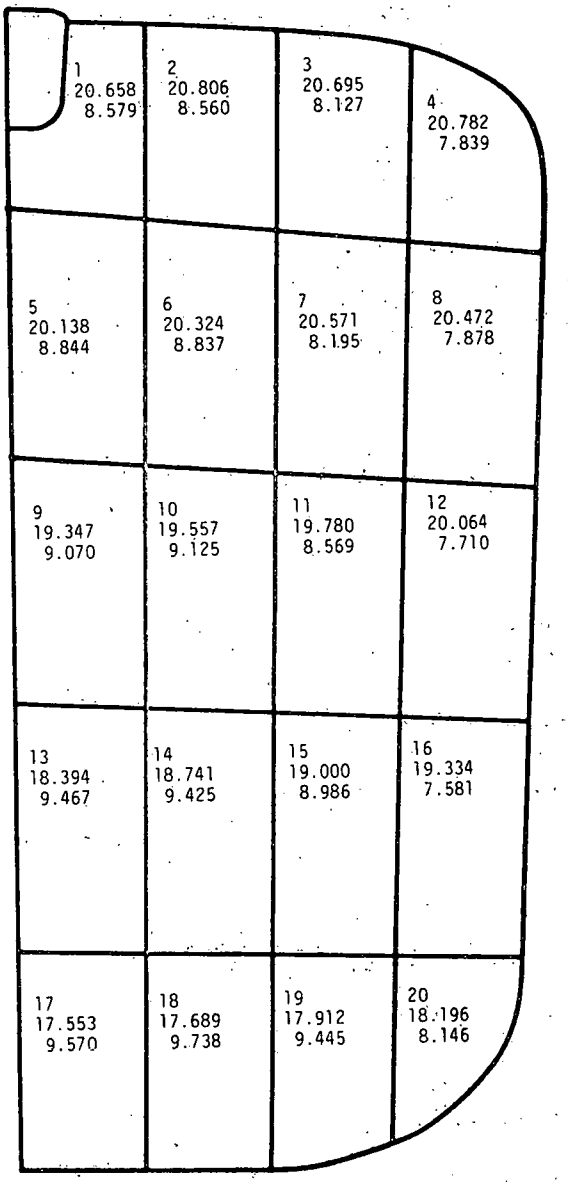

Fig. 45. Half the beam footprint at the back reflector for a beam of smaller area and more uniformity divided into subareas and showing average electric field and current density for each area.

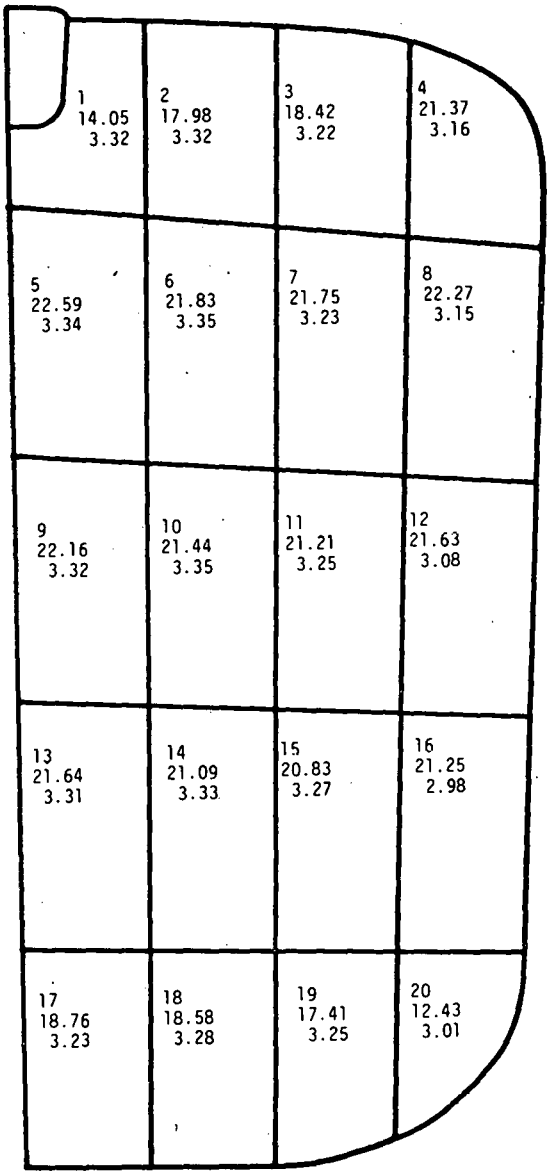

Fig. 46. Half the beam footprint at the back reflector for a beam of smaller area and more uniformity showing a number for each subarea, the area in centimeters squared of each subarea, and small signal gain at 2.2 μs.

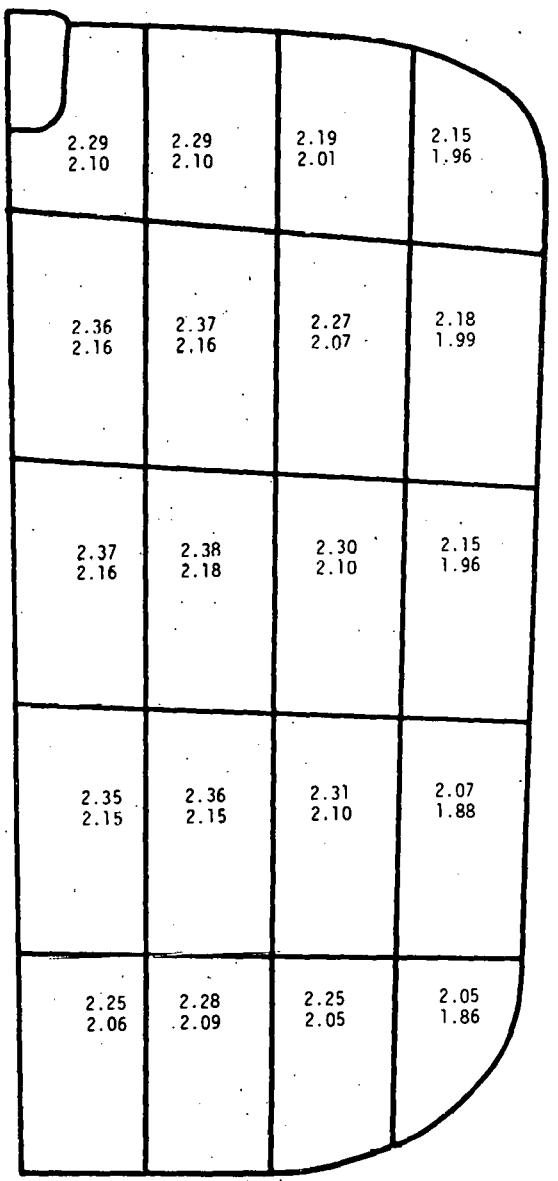

Fig. 47. Half the beam footprint at the back reflector for a beam of smaller area and more uniformity showing E(out) without and with the use of a saturable absorber. One-line extraction was used.

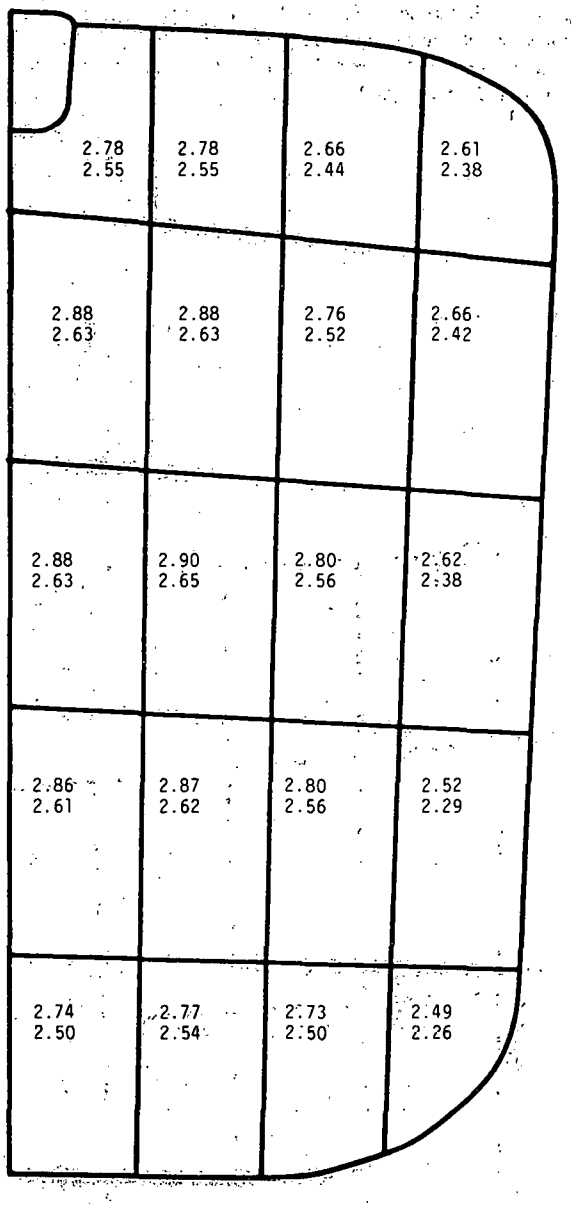

Fig. 48. Half the beam footprint at the back reflector for a beam of smaller area and more uniformity showing E(out) without and with the use of a saturable absorber. Four-line extraction was used.

TABLE XXI. Comparison of Predictions by Frantz-Nodvik and Feldman Calculations

E_{in} (J/cm^2)	E_{out} (J/cm^2)			
	One Line		Four Lines	
	F-N	Feldman	F-N	Feldman
0.124	1.21	1.23	1.44	1.46
0.484	1.93	2.29	2.35	2.59
0.516	2.13	2.72	2.80	3.05

APPENDIX

ASYMPTOTIC EXPANSION OF BESSEL FUNCTION INTEGRAL

by

Andrew B. White, Jr.

We are interested in evaluating the integral

$$\int_0^1 f(\rho)\rho\, J_0(\pi r\rho)\, d\rho \equiv F(r) \ , \tag{A-1}$$

for large values of r. First we make the change of variables $z = \pi r\rho$ to get

$$F(r) = \left[\frac{1}{\pi r}\right]^2 \int_0^{\pi r} f\left(\frac{z}{\pi r}\right) z\, J_0(z)\, dz \ . \tag{A-2}$$

We will assume further that f and all its derivatives are bounded independent of the parameter r. We will use integration by parts to devise an asymptotic expansion for F(r) that is good for $r >> 1$. From Ref. 2 (p. 484), we have

$$\int_0^z t^{\nu} J_{\nu-1}^{\nu}(t)\, dt = z^{\nu} J_{\nu}(z) \ , \tag{A-3}$$

and this identity will be used at each integration by parts. Now from Eqs. (A-2) and (A-3), we have

$$F(r) = \left[\frac{1}{\pi r}\right]^2 \left\{ \left[f\left(\frac{z}{\pi r}\right) z\, J_1(z)\right]_0^{\pi r} - \int_0^{\pi r} \frac{d}{dz}\left[F\left(\frac{z}{\pi r}\right)\right] z J_1(z)\, dz \right\} \ . \tag{A-4}$$

The integral on the right-hand side of Eq. (A-2) can itself be integrated by parts if we write

$$\int_0^{\pi r} \frac{d}{dz}\left[f\left(\frac{z}{\pi r}\right)\right] z J_1(z)\, dz \equiv \int_0^{\pi r} \frac{1}{z}\frac{d}{dz}\left[f\left(\frac{z}{\pi r}\right)\right] z^2 J_1(z)\, dz \ . \tag{A-5}$$

This leads us to further expansion of Eq. (A-4),

$$F(r) = \left[\frac{1}{\pi r}\right]^2 \left(\left\{ f\left(\frac{z}{\pi r}\right) z J_1(z) - \frac{1}{z}\frac{d}{dz}\left[f\left(\frac{z}{\pi r}\right)\right] z^2 J_2(z) \right\}_0^{\pi} + \int_0^{\pi r} \frac{d}{dz}\left\{ \frac{1}{z}\frac{d}{dz}\left[f\left(\frac{z}{\pi r}\right)\right]\right\} z^{2J}{}_2(z)\, dz \right) \ . \tag{A-6}$$

And so it goes.

By induction, we can easily show that

$$F(r) = \left[\frac{1}{\pi r}\right]^2 \left\{ \sum_{K=0}^{N} (-1)^K \left[D^K f\left(\frac{z}{\pi r}\right)\right] z^{k+1} J_{k+1}(z) \Big|_0^{\pi r} + (-1)^{N+1} \int_0^{\pi r} D^{N+1} f\left(\frac{z}{\pi r}\right) z^{N+1} J_{N+1}(z)\, dz \right\} \ , \tag{A-7}$$

where $D = (1/z)(d/dz)$. For numerical purposes, we need look only at the first two or three terms of this series.

$$D^0 f\left(\frac{z}{\pi r}\right)\, z J_1(z)\Big|_0^{\pi r} = \pi r\, f(1)\, J_1(\pi r)\ , \qquad \text{(A-8a)}$$

$$D^1 f\left(\frac{z}{\pi r}\right)\, z^2 J_2(z)\Big|_0^{\pi r} = \frac{1}{z}\,\frac{1}{\pi r}\, f'\left(\frac{z}{\pi r}\right)\, z^2 J_2(z)\Big|_0^{\pi r}$$

$$= f'(1) J_2(\pi r)\ , \qquad \text{(A-8b)}$$

and

$$D^2 f\left(\frac{z}{\pi r}\right)\, z^3 J_3(z)\Big|_0^{\pi r}$$

$$= \frac{1}{\pi r}\,[f''(1) - f'(1)]\, J_3(\pi r)\ . \qquad \text{(A-8c)}$$

Thus, we have the first three terms as

$$F(r) \sim \frac{1}{\pi r} f(1)\ J_1(\pi r) - \left[\frac{1}{\pi r}\right]^2 f'(1)\ J_2(\pi r)$$

$$+ \left[\frac{1}{\pi r}\right]^3 [f''(1) - f'(1)]\ J_3(\pi r) \qquad \text{(A-9)}$$

for large r. Since J_0 and J_1 are readily available, we can write

$$J_2(\pi r) = \frac{2}{\pi r}\ J_1(\pi r) - J_0(\pi r)\ ;$$

and we get an expression for first two terms,

$$F(r) \sim \frac{1}{\pi r}\ f(1)\ J_1(\pi r) + \left[\frac{1}{\pi r}\right]^2 f'(1)\ J_0(\pi r) \qquad \text{(A-10)}$$

as r gets large.

REFERENCES

1. J. W. Goodman, *Introduction to Fourier Optics* (McGraw-Hill, New York, 1968), pp. 63-65.

2. M. Abramowitz and I. A. Stegun, *Handbook of Mathematical Functions* (National Bureau of Standards, Washington, 1964).

3. J. D. Jackson, *Classical Electrodynamics* (J. Wiley and Sons, Inc., New York, 1962), pp. 293-294.

4. Minutes, "Antares Upgrade," Los Alamos Scientific Laboratory documents L-10/79-424, L-10/79-425, L-10/79-446, L-10/79-496, and L-10/79-497 (1979). Microfilm.

5. L. M. Frantz and J. S. Nodvik, "Theory of Pulse Propagation in a Laser Amplifier," J. Appl. Phys. **34**, 2346-2349 (1963).

6. B. J. Feldman, "Short-Pulse Multiline and Multiband Energy Extraction in High-Pressure CO_2-Laser Amplifiers," IEEE J. Quantum Electronics, **QE-9**, 1070-1078 (1973).

Printed in the United States of America
Available from
National Technical Information Service
US Department of Commerce
5285 Port Royal Road
Springfield, VA 22161

Microfiche (A01)

Page Range	NTIS Price Code	Page Range	NTIS Price Code	Page Range	NTIS Price Code	Page Range	NTIS Price Code
001-025	A02	151-175	A08	301-325	A14	451-475	A20
026-050	A03	176-200	A09	326-350	A15	476-500	A21
051-075	A04	201-225	A10	351-375	A16	501-525	A22
076-100	A05	226-250	A11	376-400	A17	526-550	A23
101-125	A06	251-275	A12	401-425	A18	551-575	A24
126-150	A07	276-300	A13	426-450	A19	576-600	A25
						601-up*	A99

*Contact NTIS for a price quote.

Los Alamos